Data and 2D scaling relations for galaxies in Abell 1689: a hint of size evolution at z~0.2

R. C. W. Houghton[1*], Roger L. Davies[1], E. Dalla Bontà[2,3], R. Masters[1]

[1] *University of Oxford, Denys Wilkinson Building, Keble Road, Oxford, OX1 3RH*
[2] *Dipartimento di Fisica e Astronomia, Università degli Studi di Padova, Vicolo dell'Osservatorio 3, I-35122, Padova, Italy*
[3] *INAF Osservatorio Astronomico di Padova, Vicolo dell'Osservatorio 5, I-35122, Padova, Italy*

ABSTRACT

We present imaging and spectroscopy of Abell 1689 (z=0.183) from the GMOS multi-object spectrograph on the Gemini-North telescope and the Advanced Camera for Surveys (ACS) on the Hubble Space Telescope (HST). We measure integrated photometry from the GMOS g′ and r′ images (for 531 galaxies) and surface photometry from the HST F625W image (for 43 galaxies) as well as velocities and velocity dispersions from the GMOS spectra (for 71 galaxies). We construct the Kormendy, Faber–Jackson and colour-magnitude relations for early-type galaxies in Abell 1689 using this data and compare them to those of the Coma cluster. We measure the intrinsic scatter of the colour–magnitude relation in Abell 1689 to be σ_{CMR} =0.054 ± 0.004 mag which places degenerate constraints on the ratio of the assembly timescale to the time available (β) and the age of the population. Making the assumption that galaxies in Abell 1689 will evolve into those of Coma over an interval of 2.26 Gyr breaks this degeneracy and limits β to be > 0.6 and the age of the red sequence to be > 5.5 Gyr (formed at $z > 0.55$). Without corrections for size evolution but accounting for magnitude cuts and selection effects, the Kormendy and Faber–Jackson relations are inconsistent and disagree at the 2σ level regarding the amount of luminosity evolution in the last 2.26 Gyr. However, after correcting for size evolution the Kormendy and Faber–Jackson relations show similar changes in luminosity (0.22 ± 0.11 mag) that are consistent with the passive evolution of the stellar populations from a single burst of star formation 10.2 ± 3.3 Gyr ago ($z = 1.8\pm^{\infty}_{0.9}$). Thus the changes in the Kormendy, Faber–Jackson and colour-magnitude relations of Abell 1689 relative to Coma all agree and suggest old galaxy populations with little or no synchronisation in the star formation histories. Furthermore, the weak evidence for size evolution in the cluster environment in the last 2.26 Gyr places interesting constraints on the possible mechanisms at work, favouring harassment or secular processes over merger scenarios.

Key words:

1 INTRODUCTION

Scaling relations for early type galaxies (ETGs) are one of the simplest tools available to study the formation and evolution of the present day population. They are particularly useful for observing changes in the stellar populations as a function of galaxy size, velocity dispersion or mass and allow us to test the conventional view that ETGs are composed of old populations which formed in a single burst of star formation some 12 – 16 Gyr (Baade 1958; Tinsley & Gunn 1976; Bruzual A. 1983; Hamilton 1985). The Faber-Jackson rela-

tion (FJR, Faber & Jackson 1976) relates the central stellar velocity dispersion (σ) to the absolute magnitude or luminosity of a galaxy,

$$M = \alpha_{\mathrm{FJR}}\log\sigma + \beta_{\mathrm{FJR}}. \qquad (1)$$

Likewise, the Kormendy relation (KR, Kormendy 1977; Hamabe & Kormendy 1987) relates the effective radius (R_e) to the surface brightness of the galaxy (μ_e),

$$\langle\mu\rangle_e = \alpha_{\mathrm{KR}}\log R_e + \beta_{\mathrm{KR}}. \qquad (2)$$

The original Kormendy relation was defined between the surface brightness *at* R_e and R_e itself. It is now conventional to use the *average* surface brightness *within* R_e against R_e.

* Email: rcwh@astro.ox.ac.uk

For a de Vaucouleurs light profile (de Vaucouleurs 1953), these are related by a constant factor, but for a Sérsic profile (Sérsic 1963) this is not the case and the conversion depends on the Sérsic index n.

Both the FJR and the KR are projections of the Fundamental plane of ETGs (FP: Dressler et al. 1987; Djorgovski & Davis 1987), linking R_e, σ and $\langle \mu_e \rangle$ (sometimes expressed in $L_\odot pc^{-2}$ as $\langle I \rangle_e$).

$$\log R_e = \alpha_{\mathrm{FP}}\log\sigma + \beta_{\mathrm{FP}}\langle\mu\rangle_e + \gamma_{\mathrm{FP}} \qquad (3)$$

The FP is tilted compared to the Virial Theorem prediction which is thought to be caused by a variation in mass-to-light (M/L) with mass (Faber et al. 1987; Renzini & Ciotti 1993).

The colour-magnitude relation (CMR, Sandage 1972) is a tight relation between the (red) colour of ETGs and their magnitude (or luminosity). Defining generic variables m_b and m_r for the magnitudes in the blue and red filters respectively,

$$m_b - m_r = \alpha_{\mathrm{CMR}}\mathcal{M}_r + \beta_{\mathrm{CMR}}. \qquad (4)$$

where $\mathcal{M}$ refers to the absolute magnitude.

1.1 Evolution in slope and intercept of scaling relations

Studying scaling relations at earlier cosmic times allows us to study the evolution of the stellar populations. Under the assumption that all galaxies evolve uniformly in brightness from the changes in stellar populations, one should observe a change in the zeropoint, β. For the FJR, the non-local relation becomes

$$\mathcal{M}_z = \alpha_{\mathrm{FJR}}\log\sigma_z + \beta_{\mathrm{FJR}} + \Delta\beta_{\mathrm{FJR}}. \qquad (5)$$

where $\mathcal{M}_z$ and σ_z are the non-local measurements and $\Delta\beta_{\mathrm{FJR}}$ represents the difference in luminosity from the local sample. Similarly for the KR,

$$\langle\mu\rangle_{e,z} = \alpha_{\mathrm{KR}}\log R_{e,z} + \beta_{\mathrm{KR}} + \Delta\beta_{\mathrm{KR}}. \qquad (6)$$

Studies of the KR at intermediate redshift show changes in $\Delta\beta_{\mathrm{KR}}$ consistent with ETGs becoming more luminous with lookback time and the slope generally appears to be unchanged (Barrientos et al. 1996; Pahre et al. 1996; Schade et al. 1996, 1997; Ziegler et al. 1999; La Barbera et al. 2003; Fritz et al. 2005; Holden et al. 2005). Similar conclusions are drawn from the evolution of the FJR (Bender et al. 1996; Ziegler et al. 2001, 2005; Fritz et al. 2005) and the FP (van Dokkum & Franx 1996a; van Dokkum et al. 1998; Treu et al. 2001; Kelson et al. 2000; van Dokkum et al. 2001; van Dokkum & Ellis 2003; Fritz et al. 2005; Holden et al. 2005; van der Wel et al. 2005; Moran et al. 2005; Jørgensen et al. 2006; Barr et al. 2006; van Dokkum & van der Marel 2007; van der Wel et al. 2006; van der Marel & van Dokkum 2007; Fritz et al. 2009; Holden et al. 2010; Saglia et al. 2010).

An important use of scaling relations was demonstrated by Kodama & Arimoto (1997) who broke the age–metallicity degeneracy (Worthey 1994) by showing that the CMR slope is the same in clusters at $z \sim 0.2$–0.4 and must originate from a variation in metallicity with luminosity,

rather than age (in that respect, the cluster ETGs were found to be coeval and old).

Recently there has been debate over the observation of downsizing (Cowie et al. 1996; Thomas et al. 2005) and the role of selection effects: the study of Holden et al. (2010) at $z \sim 0.8$ found no evidence that the tilt of the high-z FP changes from its local value, which implies that the findings of Jørgensen et al. (2006), Fritz et al. (2009) and Saglia et al. (2010) are biased by selection effects.

We emphasise the importance of updating local scaling relations with the latest technology, techniques and cosmology in relation to observations at higher redshift – the vast majority of KR, FJR and FP studies compare high redshift observations to the 15 yr old Gunn r-band observations of Jørgensen et al. (1996) and observations in different bands are even older (see the review by D'Onofrio et al. 2006). Although potentially a good reference, the SDSS FP parameters (Bernardi et al. 2003) have not been used due to their disparity with other work.

1.2 Scatter in the CMR

Bower et al. (1992, hereafter BLE92) first used the U-V Colour–Magnitude Diagram (CMD) of the Coma cluster to place constraints on the star formation histories (SFHs) of the galaxies. They estimated the scatter in the red sequence (RS) of the Coma CMD to be $\sim$0.04 mag, which can then be used to infer that either: a) all the galaxies in Coma formed at high redshift (z>2) but randomly over the preceding interval, or b) the galaxies in Coma formed more recently but were highly coeval, thus demonstrating a remarkable degree of synchronisation. Given that if all the galaxies formed at z$\sim$1, the star formation would have been apparent with moderately deep surveys and had not been observed, the authors concluded that the ETGs in Coma formed at z>2 with little synchronisation in the SFHs.

By considering the effects of more complex stellar populations (CSPs), Bower et al. (1998, hereafter BKT98) confirmed the original conclusion of BLE92. They also investigated the effects of merging on the RS and found that the small scatter of the CMR requires that the cluster galaxies formed in mass *sub-units* not much smaller than half their present day mass.

Stanford et al. (1995), Ellis et al. (1997), Stanford et al. (1998) and Mei et al. (2009), have studied many clusters with $z \lesssim 1.3$ to address evolution of the CMR scatter. They all found remarkably constant scatter, generally consistent with that of Coma with values < 0.1 mag. This implies that the bulk of the stars in these cluster ETGs are very old and formed at $z > 2$ with little synchronisation in the SFHs, although Stanford et al. and Mei et al. highlight the possibility of progenitor bias. Mei et al. also found evidence that the scatter is less for more luminous galaxies, suggesting more massive galaxies are slightly older (by $\sim$ 0.5 Gyr). We note that Stanford et al. (1998) discuss a gap in the estimates of the CMR scatter between $0.1 < z < 0.3$ which, together with their slightly higher CMR scatter at $z > 0.3$, led them to suggest possible evolution of the CMR scatter during this epoch.

1.3 This study

The evolution of the KR, FJR, FP and CMR appears to be consistent with passive fading of the stellar population from a single burst of star formation at $z > 1$. Similarly, the current evidence from analysis of the CMR is also greatly in favour of the simple passive fading of ETGs. However, simultaneous study of multiple scaling relations is rarely performed and it is unclear if they are all *quantitatively* consistent. Furthermore, it is important to account for magnitude cuts and selection effects given the results of Holden et al. (2010).

In this paper we present data and analysis techniques for the cluster Abell 1689. We compare the 2D scaling relations (CMR, KR and FJR) for Abell 1689 to those of the local cluster Coma, accounting for magnitude cuts and selection effects, and specifically testing for consistency: if the evolution of different scaling relations is governed solely by luminosity evolution of the stellar populations, they should all agree. Note that we will present the FP of Abell 1689 in a future paper. Abell 1689 is a massive cluster at z=0.183 (Struble & Rood 1999) with an X-ray luminosity of 20.74×10^{44} erg s^{-1} (Ebeling et al. 1996) making it one of the most X-ray luminous galaxy clusters known (the X-ray luminosity for Coma is 7.21×10^{44} erg s^{-1}, Ebeling et al. 1996). The KR, FJR, FP and CMR have not been previously studied in regard to the passive fading of ETGs despite it being one of the main targets for HST lensing surveys. We present colours and magnitudes for 531 galaxies, as well as spectroscopic data for 71 galaxies and surface photometry for 43 galaxies with which we investigate the CMR, KR and FJR.

Throughout this work, we adopt a WMAP7 Cosmology (Komatsu et al. 2011); specifically, we use $H_0 = 71$km s^{-1} Mpc^{-1}, $\Omega_{\mathrm{m}} = 0.27$ and $\Omega_\Lambda = 0.73$. All quoted uncertainties are standard (1σ, 68%) unless otherwise stated. The structure of this paper is as follows. In §2 we discuss the data reduction of the GMOS imaging, GMOS spectra and HST imaging as well as the data analysis techniques for the photometry and the kinematics and end with a discussion of how we fit the 2D scaling relations. Then in §3 we present our results and discuss the use of stellar population models to interpret them in §4. In §5 we present the discussion and conclude in §6. We also present Appendices regarding the data reduction and analysis: Appendix A discusses our curve-of-growth (COG) technique and the associated error analysis; Appendix B discusses how we matched the spectral profile of the stellar library to that of the GMOS-N instrument, and Appendix C presents the techniques used to fit and compare the scaling relations of Abell 1689.

2 DATA REDUCTION AND ANALYSIS

We now describe the reduction and analysis techniques used to measure integrated photometry (from GMOS-N *g_G0301* and *r_G0303* imaging, hereafter referred to as g′ and r′), surface photometry (from HST/ACS F625W imaging), and kinematics (from GMOS-N MOS).

2.1 GEMINI/GMOS imaging

Details of the seeing limited images of Abell 1689 are given in Table 1. The g′-band images have a plate scale of 0″1454 per pixel (2x2 binning) while the r′-band images have a plate scale of 0″0727 (no binning). The reduction of the GMOS imaging was based on that of Jørgensen et al. (2005) and Barr et al. (2005) but with a few differences. We use custom modified versions of the Gemini IRAF data reduction software (v1.14) and for completeness, we outline our method below.

2.1.1 Preliminary stages: bias subtraction, mosaicing and interpolation

We first processed the GMOS CCD images by performing the bias subtraction using the overscan region. A flat field image was created using a series of scaled twilight exposures (of differing exposure times) which was then applied to the Abell 1689 images. The individual chips were mosaiced onto a single image using 'nearest' interpolation to avoid correlating pixels (the error in nearest interpolation is at most half the pixel size which in this case is less than 10% of the seeing width, see also §2.5). All these processing s.ps were performed with GIREDUCE, which makes use of GPREPARE.

2.1.2 Scattered light removal

Before mosaicing the images with GMOSAIC and subtracting the residual scattered light, the background (sky and scattered light) levels on each chip were estimated (using the modal value) and equalised (individual chip levels subtracted, mean level added). However, both the g′- and r′-band images show a non-uniform scattered light pattern across the three CCD chips.

We produced a stacked scattered light frame following the recipe described in Jørgensen et al. (2005), but to prevent removal of the intra-cluster light (ICL) a 4th order polynomial surface was fit to the frame, one chip at a time, to provide a smooth representation of the scattered light while leaving the ICL present. As in Jørgensen et al. (2005), we scaled the scattered light frame (a polynomial surface in our case) by between 0.8 and 1.2 (in 0.05 intervals) and determined the best subtraction by eye for each frame.

The scattered light corrected frames were then aligned, scaled and combined using a modified version of the IMCOADD routine (allowing multiple pointings to be combined into a single mosaic). The default intensity scaling of individual images by IMCOADD (given by the header keyword RELINT) was found to be unreliable; instead, we fitted a Moffat function to a star present in the overlapping pointings of all images, and used the flux within 3 FWHM to scale each of the images to a common standard.

2.1.3 Flux calibration

Flux calibration of the g′-band images followed the prescription in Jørgensen (2009) and final zeropoints are listed in Table 2. We used standards from Landolt (1992) or Landolt & Uomoto (2007) to estimate the zero points (ZP) for each night.
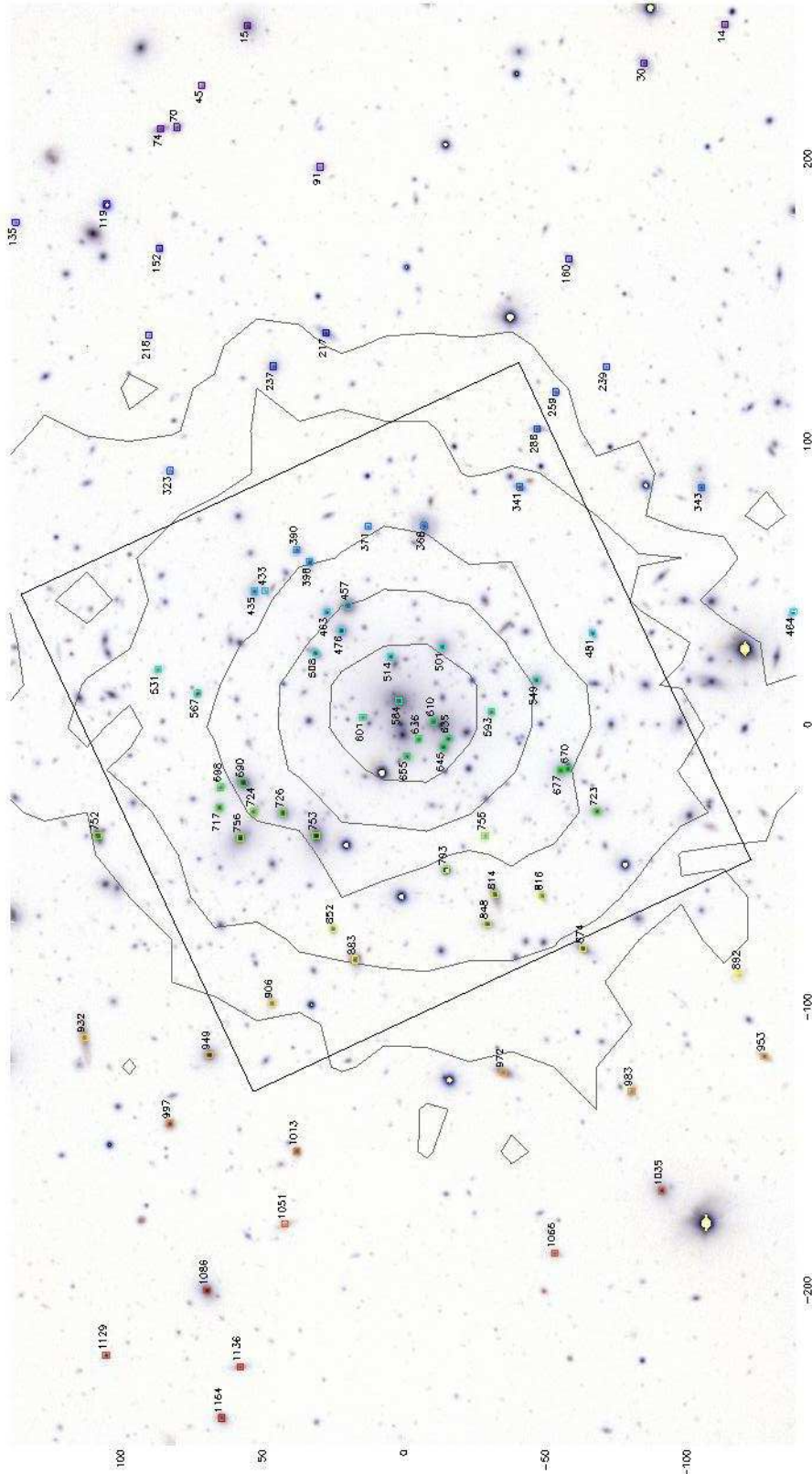
Figure 1. A negative image of the galaxy cluster Abell 1689 observed using the g′- and r′-band filters with the GEMINI/GMOS imager. The g′-band image has been degraded to match the resolution of the r′-band image. Overlaid is the HST footprint (solid black square) and the ROSAT X-ray map (grey, solid lines; contours were shifted by {-0.008,-0.006} degrees in {RA,DEC} to align with the cluster core). Coloured squares mark the galaxies in the spectroscopic sample, apart from #119, #793, #1129 which are guiding/alignment stars. Note that #160, #457, #892, #932, #983 and #1051 are not in the cluster potential according to their recession velocities (see Table 6).
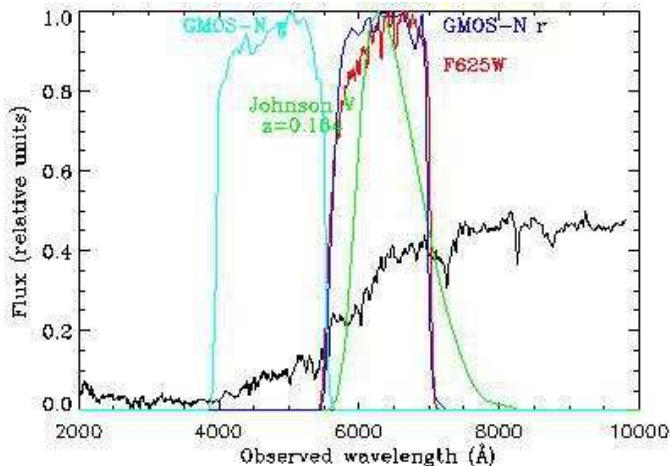
Figure 2. The GMOS-N filters transmission curves (g′, r′) together with the HST/ACS F625W transmission curve are shown together with a galaxy template spectrum (Santos et al. 2001) which has been redshifted to z=0.183. Also shown for comparison is a standard Johnson V-band filter curve (Bessell 1990, photographic, from) in the rest frame of the galaxy spectrum.

The g′-data was all taken during photometric conditions and with good seeing ($\sim 0{.}''6$ in the combined image); consequently, the images required little relative scaling. The photometric standard was taken minutes after the last exposure, minimising systematic error from atmospheric changes. We scaled all images to the last image of the night, which was nearest in time to the observation of the photometric standard and also had one of the highest relative throughputs of all the images (see Table 2).

The r′-band data were taken over two consecutive nights, the first of which was not photometric while the second was. From the relative throughput of the images, it is clear that the flux in the photometric images of the second night varies only by a few percent compared to the non-photometric images of the first night, and we scaled all images to the brightest photometric image of the second night (with airmass <1.2) and flux calibrated the images using an average of the ZPs derived from all standards. We also scaled the science images to correct for airmass (according to Jørgensen 2009). The ZPs in Table 2 do not include a term for the extinction from the Galaxy. For the coordinates of Abell 1689, $A_g = 0.106$ and $A_r = 0.075$ (Schlegel et al. 1998; Cardelli et al. 1989): these corrections are applied to all integrated (§2.3) and surface photometry (§2.3.1) measurements.

2.2 HST imaging

We used *HST*/ACS images of Abell 1689 obtained with the Wide Field Channel (WFC) as part of the ACS Guaranteed Time Observation program 9289 (P.I. H. Ford). The WFC detector consists of two 4096×2048 SITe CCDs butted together along their long dimension and separated by a gap corresponding to approximately 50 pixels (2.5 arcsec). The plate scale is 0.050 arcsec pixel^{-1}. Each chip uses two amplifiers to read a single 2048×2048 quadrant. We downloaded from the public *HST* archive the images employing the F625W filter, which resembles the SDSS/GMOS r′ filter

(see Fig. 2). The observations were carried out on 14 June 2002 and consist of eight exposures (four pointings split in two to deal with cosmic rays) for a total integration time of 9500 sec. The dithered images were able to cover the gap between the adjacent chips.

All images were calibrated using the standard reduction pipeline PYRAF/CALACS maintained by the Space Telescope Science Institute. Reduction steps include bias subtraction, dark current subtraction, and flat fielding, as described in detail in the ACS instrument (Maybhate A., et al. 2010) and data (Pavlovsky C., et al. 2004) handbooks.

We used PYRAF task MULTIDRIZZLE together with standard tasks in IRAF[1] to combine all exposures into a single geometrically corrected image while rejecting cosmic rays. We let MULTIDRIZZLE generate the inverse-variance weighting map automatically, which is suitable for SExtractor (Bertin & Arnouts 1996). We analyzed the images obtained with different kernels by comparing the point spread function (PSF) FWHM derived fitting a two-dimensional Gaussian to a few stars distributed in the field of view. We chose to use the square drizzle kernel. In addition, for the photometric analysis we need a well sampled PSF. The most suitable values for scale and pixfrac were found to be 0.030 arcsec pixel^{-1} and 1.0, respectively. Prior to MULTIDRIZZLE, we processed every flat-fielded image by fitting a sky level in each quadrant separately, as suggested by Sirianni et al. (2005), because of residual differences after the bias subtraction.

The final, combined, and geometrically corrected image has a size of 7062×7251 pixel^2, with 0.030 arcsec pixel^{-1}. The resulting field of view is approximately $212'' \times 218''$ in the shape of a rhomboid.

The transformation to the AB photometric system follows Sirianni et al. (2005). We adopted the photometric keywords tabulated in the header of the images, as suggested by Pavlovsky C., et al. (2004) to ensure up-to-date values based on the throughput curves of all *HST* optical components:

$$r_{\rm AB} = -2.5 \log f({\rm F625W}) + 25.9186, \qquad (7)$$

where $f({\rm F625W})$ refers to the integrated flux in units of electrons per second.

We produced a suitable PSF for each sample galaxy included in the *HST* image. The aim is to obtain realistic PSFs that underwent the same reduction-steps we performed on the observed images. The method is similar to the one adopted by Chiboucas et al. (2009). For each galaxy we derived from the flat-fielded images the coordinates in pixel of its centre. By using the TINYTIM package (Krist & Hook 1999) we produced PSFs corresponding to all the exposures. We created TINYTIM PSFs with a diameter of 3 arcsec. The PSFs were added to synthetic images equal to the flat-fielded ones, but with pixel values set to zero. These were then combined, aligned, and corrected for geometric distortion in the same way as the real images. Finally, we extracted

---

[1] IRAF is distributed by the National Optical Astronomy Observatories which are operated by the Association of Universities for Research in Astronomy (AURA) under cooperative agreement with the National Science Foundation.

Filename	Airmass sec(z)	Moffat FWHM	Gaussian FWHM	Scaling	Relative Throughput	Filter	Obs. Time (UT)	Exp. Time (s)
N20031224S0065	1.327	$0\rlap{.}''56$	$0\rlap{.}''619$	1.059	0.971	g'	14:57:29	180
N20031224S0066	1.311	$0\rlap{.}''53$	$0\rlap{.}''583$	1.062	0.964	g'	15:01:24	180
N20031224S0067	1.295	$0\rlap{.}''53$	$0\rlap{.}''593$	1.060	0.962	g'	15:05:20	180
N20031224S0068	1.281	$0\rlap{.}''52$	$0\rlap{.}''585$	1.059	0.960	g'	15:09:14	180
N20031224S0070	1.243	$0\rlap{.}''57$	$0\rlap{.}''597$	1.006	1.001	g'	15:20:09	180
N20031224S0071	1.231	$0\rlap{.}''54$	$0\rlap{.}''610$	1.009	0.995	g'	15:24:04	180
N20031224S0072	1.219	$0\rlap{.}''52$	$0\rlap{.}''600$	1.000	1.000	g'	15:28:00	180
N20031224S0073	1.208	$0\rlap{.}''50$	$0\rlap{.}''580$	1.000	0.998	g'	15:31:54	180
Coadded g'-band	1.219	$0\rlap{.}''56$	$0\rlap{.}''607$	1.000	1.000	g'	-	1440
N20011223S174	1.310	$1\rlap{.}''13$	$1\rlap{.}''159$	1.005	1.031	r'	15:01:09	300
N20011223S175	1.279	$1\rlap{.}''08$	$1\rlap{.}''164$	1.009	1.020	r'	15:09:12	300
N20011223S176	1.252	$1\rlap{.}''07$	$1\rlap{.}''147$	1.007	1.015	r'	15:17:14	300
N20011223S178	1.213	$1\rlap{.}''08$	$1\rlap{.}''118$	1.012	1.000	r'	15:29:56	300
N20011223S179	1.191	$1\rlap{.}''14$	$1\rlap{.}''246$	1.012	0.994	r'	15:38:10	300
N20011223S180	1.172	$1\rlap{.}''02$	$1\rlap{.}''066$	1.009	0.992	r'	15:46:14	300
N20011224S139	1.518	$1\rlap{.}''25$	$1\rlap{.}''158$	1.021	1.071	r'	14:17:41	300
N20011224S140	1.466	$1\rlap{.}''30$	$1\rlap{.}''134$	1.015	1.063	r'	14:25:54	300
N20011224S149	1.167	$0\rlap{.}''85$	$0\rlap{.}''864$	1.000	1.000	r'	15:44:19	300
N20011224S150	1.150	$0\rlap{.}''88$	$0\rlap{.}''997$	1.007	0.989	r'	15:52:22	300
N20011224S151	1.135	-	-	-	-	r'	16:00:28	300
Coadded r'-band	1.167	$1\rlap{.}''06$	$0\rlap{.}''936$	1.000	1.000	r'	-	3000

Table 1. The GEMINI/GMOS imaging data. The g'-band data were observed with a plate scale of $0\rlap{.}''1454$ (2x2 binning) while the r'-band data were observed with a plate scale of $0\rlap{.}''0727$ (1x1 binning). The last exposure in the r'-band was badly affected by twilight and was rejected because the scattered light pattern could not be adequately subtracted off. Images are scaled to the exposure nearest in time to the observation of the photometric standard (see Table 2)

Filename	Object Name	Airmass sec(z)	Exp. Time (s)	Obs. Time (HH:MM:SS)	Counts (e^-/s)	m_{std} (mag)	m_{ZP} (mag)	Filter
N20031224S0081	PG1323-086	1.241	3	16:06:09	6.17×10^5	13.335^a	27.844	g'
N20031224S0082	PG1323-086	1.239	3	16:06:58	6.38×10^5	$13.335^a,13.283^c$	27.881	g'
N20031224S0083	PG1323-086	1.237	1	16:07:49	6.00e5	$13.335^a,13.283^c$	27.814	g'
N20031224S0084	PG1323-086	1.235	1	16:08:36	6.24e5	$13.335^a,13.283^c$	27.856	g'
N20011223S119	G191B2B	1.197	5	09:42:04	24.90×10^5	12.044^b	28.062	r'
N20011224S153	PG1323-086	1.219	1	06:09:38	4.93×10^5	$13.663^a,13.660^c$	27.919	r'
N20011224S154	PG1323-086	1.216	1	06:09:38	5.25×10^5	$13.663^a,13.660^c$	27.987	r'

Table 2. The GEMINI/GMOS imaging standards used to calibrate the photometry used here. Note that the g'-band standards were observed straight after the science observations, while the r'-band standards were observed some hours before hand (see Table 1). Zero points (ZP) were calculated according to the prescription of Jørgensen (2009). Magnitudes for the photometric standards (m_{std}) were calculated using the $f(B, B - V)$ transformation in Smith et al. (2002) and the data from either Landolt (suffix a, 1992) or Landolt & Uomoto (suffix b, 2007); magnitudes for these standards calculated by Jørgensen (2009) are also given (suffix c). The average ZP from the above standards for the g'-band data is 27.85±0.03 while the average ZP for the r'-band is 27.99±0.07.

the PSF from the processed image, with a pixel scale of 0.03 arcsec pixel^{-1}.

2.3 Integrated Photometry

We used SExtractor on the GMOS g'- and r'-band images to calculate the integrated magnitudes in those filters. We selected galaxies using the g' image (it has better seeing than the r' image, see Table 1) to be above a threshold of 3 times the sky noise and have a minimum area of 8 pixels. A total of 64 de-blending sub-thresholds were permitted with a minimum contrast of 1×10^{-4}. No filter was applied for detection.

When running SExtractor in *dual image mode*, the images must be identically aligned, scaled, sampled and PSF convolved. We re-binned and aligned the r'-band image to match the g'-band image and degraded the g'-band resolution to that of the r'-band by convolving with a Gaussian (FWHM=$0\rlap{.}''877^2$). A pseudo-colour image of Abell 1689 using the g'- and r'-band images is presented in Fig. 1.

We extract total (MAG_AUTO: based on the Kron definition) and fixed circular aperture magnitudes (MAG_AP: diameter of $2\rlap{.}''9$) for all detected objects. This aperture size

---
[2] This number is found by trial and error to give similar Gaussian fits to both the g'- and r'-band images.

was chosen because it is approximately three times the Gaussian FWHM of the seeing disc in the r′ image and exactly 20 pixels. From the aperture magnitudes in g′ and r′, we calculate the g′-r′ colour of the galaxies.

The errors produced by SExtractor when using just the input science images appeared to be underestimated. Instead, when provided with a variance image to act as a weight map (produced by the GMOS pipeline with stars masked), SExtractor produced more realistic errors, used here.

We present the colour-magnitude diagram in Fig. 3: the r′ magnitude represents the total (Kron) magnitude while the g′-r′ colour is derived from the aperture magnitudes. To use only reliable photometry of galaxies, we select data where: the errors on magnitudes are less than 0.1 mag; total magnitudes are brighter than 25 mag in g′ and r′; SExtractor has not flagged the photometry for any reason[3]); the object was not identified as a star (CLASS_STAR < 0.99) and the object has a FWHM> 4 pixels. Note that the error ellipses neglect the correlation between the r′-band aperture and total magnitudes. This data is further presented in §3.1 and discussed in §5.1. We show the constraints for spectroscopic sample selection as dotted lines, which are discussed in §2.5.

2.3.1 Surface Photometry

There are two common approaches to calculating the effective radius r_e and the average surface brightness within r_e, $\langle\mu\rangle_e$ from the flux calibrated images: curve-of-growth fitting (COG, e.g. Dressler et al. 1987; Jørgensen et al. 1992) and differential surface fitting (e.g. GASP2D Méndez-Abreu et al. 2008). The COG technique was originally used to parameterise the scale and brightness of galaxies, assuming a de Vaucouleurs like profile for all galaxies, where the surface brightness $I(R)$ is defined to be

$$I(R) = I_0\exp\left(-7.676[R/R_e]^{1/4}\right). \qquad (8)$$

However, more recently the differential fitting technique has been more widely used in the literature (e.g. van Dokkum & Franx 1996b); furthermore it has become common to fit the more general Sérsic model (for which the de Vaucouleurs profile is a special case), defined as

$$I(R) = I_0\exp\left(-b[R/R_e]^{1/n}\right). \qquad (9)$$

where $b \approx 2n - 0.324$ over the range $2 < n < 10$ (Ciotti 1991). Recall also that the intensity *at* R_e is $I_e = I_0\exp(-b)$ and the average intensity within R_e is $\langle I\rangle_e = I_e\exp(b)\Gamma(2n)nb^{-2n}$ where Γ is the gamma function.

We chose to use the older COG technique for consistency with the majority of earlier work on scaling relations and fit both de Vaucouleurs and Sérsic profiles, for which the integrated luminosity increases with projected radius as

$$L(R) = I_0 R_e^2 \frac{2\pi n}{b^{2n}}\gamma[b(R/R_e)^{1/n}, 2n] \qquad (10)$$

where γ is the incomplete gamma function (Ciotti 1991).

In a future paper we will compare these results with full surface fitting and decomposition methods. We developed our own curve-of-growth (COG) software (written in IDL) and implemented this software on the HST/ACS F625W image for the spectroscopic sample. This limited the final sample which could enter our analysis: we observed a total of 77 galaxies in the spectroscopic sample and while all these galaxies have ground-based g′- and r′-band imaging (§2.1), the HST image covers only 43 of the original 77 galaxies.

Details of the COG algorithm (including masking of nearby sources, correction of PSF effects) are given in Appendix A. We use Monte-Carlo simulations of the fitting procedure, to estimate the random and systematic uncertainties in $\log R_e$ and $\log I_e$. These simulations include photon shot noise, typical systematic errors in the subtracted sky level and a suitable range of radii over which we fit model COGs (see Appendix A). We calculate the covariance terms for use when fitting the scaling relations (see §2.9) and plotting error ellipses in §3. Both the de Vaucouleurs and Sérsic COG surface photometry are given in Table 4; $\langle\mu\rangle_e$ has been corrected for cosmological dimming and $\log R_e$ is given in kpc (assuming the cosmology described in §1).

2.4 Photometric accuracy

We perform a number of cross-checks to ensure the accuracy of our photometry. The results of these checks are discussed below and when (internally) comparing the derived magnitudes of the galaxies we quote the mean difference and the RMS scatter in the relation.

We check the GMOS r′-band ZP in two ways: firstly we compare the magnitude of an unsaturated star in our field (RA=13:11:33.5, DEC=-01:20:44.7) to the same stars observed with SDSS; we measure an r′ magnitude of 17.12 while SDSS quotes an r ′ magnitude of 17.150 ± 0.005 (unfortunately the same star is saturated in the g′-band due to better seeing).

We also check how consistent the de Vaucouleurs and Sérsic COG magnitudes are: a direct comparison in the HST F625W image indicated that the Sérsic magnitudes were 0.06 mag fainter than the de Vaucouleurs magnitudes (with 0.2 mag scatter; the median difference was also 0.06 mag).

Finally we compare the GMOS r′ SExtractor magnitudes to the HST r′ COG magnitudes: we find the SExtractor Kron magnitudes are fainter than the de Vaucouleurs magnitudes by 0.12 mag (with 0.20 mag scatter and median of 0.17 mag) and fainter than the Sérsic magnitudes by 0.08 mag (with 0.22 mag scatter and median of 0.13 mag). We estimate that the HST F625W and GMOS r′ images are calibrated to better than 0.1 mag (the scatter in the r′ zeropoints in Table 2 is 0.07 mag). We believe the remaining difference is because SExtractor (Kron) magnitudes are not extrapolated to infinity. In principle, we could generate simulations to test this, but feel it is not central to our analysis because any uncertainty in the GMOS r′ calibration has little bearing on the results, as we use the scatter in the CMR derived from the GMOS r′ SExtractor catalogue, which is independent of the zeropoint.

---

[3] other than flags 1 and 2 which inform if the photometry was biased by nearby bright objects or originally blended with a neighbour, respectively.

Table 3. The SEXTRACTOR photometry of the GMOS r′ and g′ images. The *Phot. ID* is the identification from SEXTRACTOR (which we find no need to quote other than in this table), while the *Spec. ID* is the ID in the spectroscopic sample (which *is* quoted in this paper when referring to a galaxy or star). R.A. and DEC. are given in degrees and are calculated from the g′ GMOS image coordinates. The *Red Seq.* column informs us if the object is more likely to be in the red sequence (Y=yes) than not (N=No; i.e. it is more likely to be in the outlier distribution) using the results of the mixture model (see §2.9, §3.1 & §C). The apparent r′ magnitudes and the g′-r′ colours have been corrected for extinction (atmospheric and Galactic). We refer the reader to the SEXTRACTOR manual for further information on the flag codes (v.2.13, §9.1, p28). Note that the g′-r′ colour is an aperture magnitude while the r′ magnitude is a Kron (total) magnitude. Note also that galaxy #655 does not meet the criterion specified in §2.3, but we include it here for completeness (it *is* included in the KR and FJR). *The full table appears in the online version.*

Phot. ID	Spec. ID	R.A. (deg)	DEC. (deg)	Red Seq.	r′ (mag)	g′-r′ (mag)	r′ flag	g′ flag
154	14	197.8058167	-1.3739161	Y	19.2334±0.0014	0.9509±0.0008	2	2
1364	15	197.8058014	-1.3269255	Y	17.7165±0.0007	0.9600±0.0004	2	2
261	30	197.8095551	-1.3659689	Y	18.5313±0.0011	0.9600±0.0006	2	2
1317	45	197.8116913	-1.3224429	Y	20.0542±0.0021	0.9136±0.0013	0	0
1213	70	197.8158112	-1.3199574	Y	18.9672±0.0009	0.9675±0.0007	3	3
1217	74	197.8159485	-1.3183731	Y	18.6034±0.0008	1.0388±0.0006	3	3
1508	91	197.8197632	-1.3340420	Y	19.3286±0.0018	0.9885±0.0011	2	2
1658	135	197.8251495	-1.3040887	Y	19.6441±0.0014	0.9673±0.0014	0	0
1149	152	197.8277740	-1.3182346	Y	19.2382±0.0009	1.0686±0.0008	0	0
435	160	197.8289032	-1.3585705	N	19.5570±0.0016	0.2652±0.0007	0	0
891	217	197.8361206	-1.3346049	Y	18.2879±0.0006	1.0289±0.0004	2	2
1197	218	197.8362885	-1.3172021	Y	20.5914±0.0027	0.9489±0.0021	0	0
1430	237	197.8394165	-1.3294218	Y	18.6605±0.0009	0.9995±0.0006	2	2
385	239	197.8395233	-1.3621749	Y	20.1782±0.0019	0.9885±0.0014	0	0
471	259	197.8419952	-1.3572158	N	19.4536±0.0011	0.7208±0.0007	0	0
461	286	197.8456116	-1.3554035	Y	18.9960±0.0009	0.9863±0.0007	2	2
1237	323	197.8496857	-1.3192796	Y	19.4914±0.0016	0.9888±0.0011	2	2
520	341	197.8513641	-1.3536860	Y	18.6636±0.0007	0.9992±0.0006	3	3
...	...	...	...	...	...	...	...	...

2.5 GEMINI/GMOS-N spectroscopy

The GMOS-N instrument in multi-object spectroscopy (MOS) mode simultaneously provides multiple spectra in the range $0.35\mu m - 1.1\mu m$ inside a $5.5' \times 5.5'$ field of view (Hook et al. 2004). The spectra of 77 galaxies in Abell 1689 and 3 guide/alignment stars were taken with GMOS-N between 10th January 2002 and 15th January 2002 using the B600_G5303 grating and $0.''75$ slits, giving a resolution $R \approx 1700$ ($\sigma \approx 75$km s^{-1}) and a (observer-frame) wavelength range of approximately 3500Å to 7000Å, depending on the position in the field of view (FOV). The spectroscopic sample is bluer than $g' - r' = 1.1$ mag, redder than $g' - r' = -0.17r' + 3.4$ mag and 50% complete to $r' = 19.5$ mag (see §C2). Of the *total* number of galaxies matching these limits, around 50% are in the spectroscopic sample (but note that as a function of magnitude, we are consistent with sampling 60% of each magnitude bin, see §C2). The locations of the galaxies are shown in Fig. 1 while the selection criteria are shown on Fig. 3. The inset histogram in Fig. 1 compares the distribution of the parent sample to the total spectroscopic sample and the spectroscopic sample that is limited to the HST footprint: the total spectroscopic sample is a good representation of the parent sample, while the sample that lies in the HST footprint is slightly biased towards more luminous galaxies. Note that an apparent magnitude limit of r′ < 19.5 mag is equivalent to a rest frame absolute magnitude limit of $\mathcal{M}_V < -20.04$ mag.

Four masks were used when observing the cluster and for each mask, the data were observed with two different central wavelengths (565 nm and 570 nm) so that the two chip gaps did not cause discontinuity in the data. The number of exposures for each mask varies and details are given in Table 5. Our reduction of the spectra is initially very similar to that of the imaging (§2.1) but differs in extraction. We again follow the ideas in Jørgensen et al. (2005) and Barr et al. (2005) but with a few differences: we use custom modified versions of the Gemini IRAF data reduction software (v1.14) and for completeness, we outline our method below.

We process the CCD images in the usual manner, performing bias subtraction using the overscan region and flat field as normal. The individual chips were mosaiced onto a single image using 'nearest' interpolation, which retains the statistical independence of the pixels. This has no effect on the final result, as GMOS samples the spectral and spatial PSFs better than the Nyquist limit, by a factor of ~ 5; in practice the positioning of our data is accurate to 10% of the PSF FWHM. These processing s.ps were performed with GSREDUCE, which itself makes use of GPREPARE, GIREDUCE, GMOSAIC and GSCUT. Furthermore, a cosmic ray rejection step is present in GSREDUCE.

Most of the slits were cut at an angle so it was necessary to rectify the spectra to a uniform space and wavelength grid. This was performed with GSWAVELENGTH using a 4th-order (Legendre) polynomial fit along λ and a 2nd-order polynomial fit along the spatial axis. Residuals were typically less than 0.2 Å. The absolute zero point of the wavelength calibration required correction which was ac-
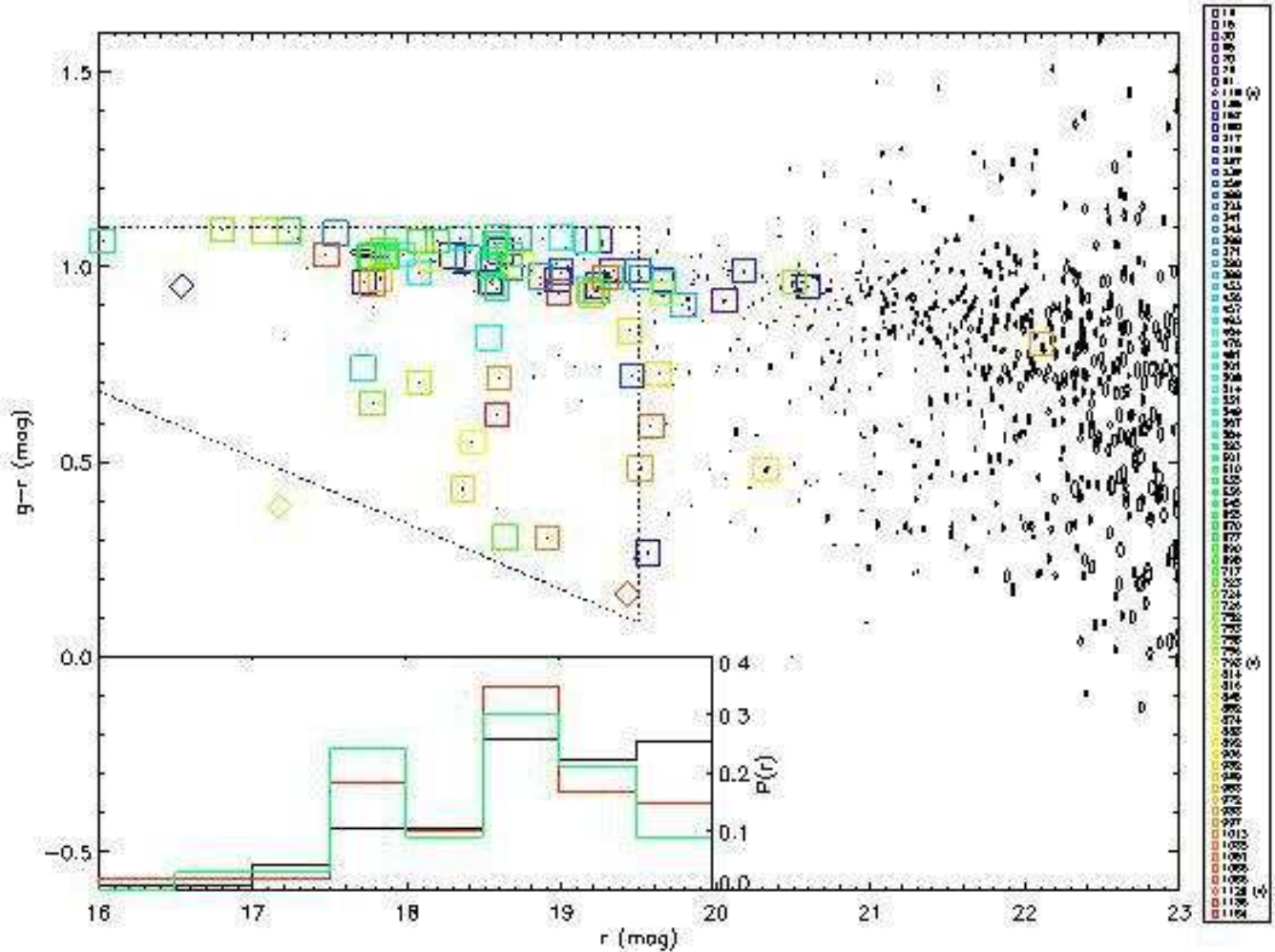
Figure 3. The Colour-Magnitude diagram for Abell 1689 created using the GEMINI/GMOS photometry with SEXTRACTOR: only data with errors less than 0.1 mag are shown. The spectroscopic galaxy sample is highlighted with coloured squares while coloured diamonds represent stars. In the legend, labels followed by a star in parenthesis are guiding/alignment stars (#119, #793, #1129); of the other diamonds, #972 is reported by SEXTRACTOR to be contaminated (the galaxy is peculiar and appears in the g-band image to have two parts) while #655 is reported by SEXTRACTOR to be a star but its spectrum confirms it to be a galaxy (as does the HST photometry). The complete sample is shown by plotting the error ellipses (often too small to distinguish from a dot). Selection limits for the spectroscopic sample (§2.5) are shown as dotted lines (r' = 19.5 mag represents 50% completeness) and the inset histogram shows the distribution of all objects brighter than r' < 20 for the parent sample (black), for the spectroscopic sample (red) and for the spectroscopic sample inside the HST footprint (green).

complished using the [OI] (5577.34 Å) and NaD (5889.95 Å, 5895.92 Å) sky lines. Our data were reduced to a log-λ grid with only one interpolation to help retain the statistical independence of the pixels and minimise correlations.

The sky was removed using GSSKYSUB and a 1D galaxy spectrum extracted using an aperture of diameter 1″.4 (4.3 kpc at z=0.183) tracing the peak flux of the galaxy spectrum. Individual 1D spectra from each exposure were combined by scaling by the median, rejecting bad pixels (including the chip gaps) and clipping the data at $\pm 5\sigma$ to remove bad pixels or cosmics that escaped earlier detection.

2.6 Kinematics

To extract the kinematics from the spectra, we assume that the galaxy spectrum G (sampled in logλ) is the convolution of a stellar template T with a distribution of stellar velocities $L(v)$,

$$G(\log\lambda) = T(\log\lambda) \otimes L(v). \qquad (11)$$

Furthermore, we assume that $L(v)$ takes the parameterised form of a Gaussian with velocity V and velocity dispersion σ.

In order for Eq. 11 to be valid, the stellar template population must match the galaxy population and both should have the same spectral resolution (i.e. they should both appear to have been observed with the same instrument). In practice, this is achieved by taking a large stellar library (such as the Indo-U.S. Library of Coudé Feed Stellar Spectra (CFLIB) used here, Valdes et al. 2004) observed at high spectral resolution and degrading it (via convolution) to match the spectral line profile of the instrument; one then

Table 4. HST F625W COG surface photometry for 43 galaxies which are also in the GMOS spectroscopic sample. Both de Vaucouleurs and Sérsic COGs were used: de Vaucouleurs parameters are headed with *(dV)* while Sérsic parameters are headed *(S)*; the Sérsic index n only appears in this table for Sérsic COG fits ($n = 4$ for de Vaucouleurs COGs). Values of $\log R_e$ are in kpc and values of $\langle\mu\rangle_e$ are corrected for extinction (atmospheric and Galactic), Tolman dimming and the bandpass term of the K-correction (assuming the cosmology described in §1). The apparent magnitudes m are calculated directly from the counts in the COG and have only been corrected for extinction, as described in §2.1.3. Uncertainties in the parameters (σ) were calculated from simulation, including the correlation coefficient between $\log R_e$ and $\langle\mu\rangle_e$ (ρ, see §2.3.1 & §A3). The flags represent the quality of the COG fits: *1* for galaxies whose COG was well represented by the model COG; *2* for galaxies whose COG was not well represented by the model COG; *3* for galaxies whose COG did not asymptotically tend to a constant value and/or had severe contamination from neighbouring galaxies such that, even after masking, were unreliable (see §A2). Only galaxies with flags *1* or *2* enter the fitting process; galaxies #584 and #610 are BCGs which were fitted in some cases (c.f. §3 and Table 7).

Spec. ID	$\log R_e$ (dV)	$\langle\mu\rangle_e$ (dV)	ρ (dV)	m (dV)	Flag (dV)	$\log R_e$ (S)	$\langle\mu\rangle_e$ (S)	ρ (S)	m (S)	n (S)	Flag (S)
286	0.40±0.35	19.79±1.10	-0.998	18.78±0.00	2	0.35±0.13	19.66±0.39	-1.000	18.86±0.00	2.8	2
341	0.37±0.35	19.34±1.10	-0.999	18.47±0.00	2	0.35±0.13	19.28±0.39	-1.000	18.52±0.00	3.2	2
368	1.02±0.34	21.37±1.10	-0.999	17.24±0.00	2	0.85±0.03	20.77±0.07	-0.999	17.50±0.00	2.0	2
371	0.40±0.35	20.38±1.10	-0.998	19.33±0.00	1	0.47±0.20	20.65±0.71	-1.000	19.24±0.00	5.2	1
390	0.41±0.35	19.74±1.10	-0.998	18.65±0.00	1	0.37±0.13	19.59±0.39	-1.000	18.71±0.00	3.2	1
398	0.25±0.35	18.87±1.10	-0.998	18.60±0.00	2	0.22±0.11	18.80±0.29	-1.000	18.67±0.00	2.6	1
433	0.70±0.37	22.11±1.13	-0.993	19.57±0.00	2	0.57±0.20	21.68±0.46	-1.000	19.77±0.00	2.0	2
435	0.63±0.35	20.62±1.10	-0.999	18.42±0.00	1	0.68±0.08	20.79±0.29	-1.000	18.36±0.00	4.9	1
463	0.60±0.35	20.45±1.10	-0.999	18.43±0.00	1	0.63±0.08	20.57±0.29	-1.000	18.38±0.00	4.8	2
476	0.44±0.35	19.17±1.10	-0.999	17.95±0.00	2	0.39±0.05	19.03±0.15	-1.000	18.03±0.00	2.8	2
481	0.25±0.35	19.31±1.10	-0.998	19.02±0.00	2	0.26±0.11	19.40±0.29	-1.000	19.08±0.00	2.4	1
501	0.82±0.35	21.01±1.10	-0.999	17.86±0.00	2	0.80±0.06	20.92±0.17	-1.000	17.91±0.00	3.3	2
508	0.57±0.35	20.16±1.10	-0.999	18.30±0.00	2	0.43±0.06	19.70±0.14	-0.999	18.50±0.00	2.2	2
514	0.45±0.35	19.83±1.10	-0.998	18.57±0.00	2	0.94±0.09	21.80±0.33	-1.000	18.06±0.00	9.8	2
531	0.35±0.35	20.27±1.10	-0.998	19.48±0.00	2	0.33±0.20	20.29±0.46	-1.000	19.59±0.00	1.8	2
549	0.66±0.35	20.45±1.10	-0.999	18.09±0.00	1	0.64±0.06	20.35±0.17	-1.000	18.13±0.00	3.5	1
567	0.12±0.35	18.64±1.10	-0.998	18.99±0.00	1	0.13±0.16	18.67±0.51	-1.000	19.00±0.00	3.6	1
584	1.48±0.34	22.07±1.09	-0.999	15.62±0.00	3	0.99±0.00	20.47±0.01	-0.998	16.48±0.00	1.2	3
593	0.25±0.35	19.55±1.10	-0.998	19.27±0.00	1	0.25±0.16	19.58±0.51	-1.000	19.27±0.00	3.7	2
601	0.56±0.35	21.01±1.10	-0.998	19.16±0.00	2	0.46±0.13	20.65±0.39	-1.000	19.30±0.00	2.9	1
610	1.04±0.34	20.99±1.10	-0.999	16.77±0.00	3	1.05±0.03	21.03±0.08	-1.000	16.76±0.00	3.9	3
635	0.63±0.35	20.25±1.10	-0.999	18.05±0.00	3	0.78±0.09	20.83±0.33	-1.000	17.87±0.00	5.9	3
636	0.59±0.35	20.68±1.10	-0.998	18.72±0.00	3	0.70±0.31	21.13±1.14	-1.000	18.61±0.00	6.2	3
645	0.60±0.35	20.02±1.10	-0.999	17.97±0.00	2	0.55±0.04	19.83±0.11	-1.000	18.06±0.00	2.6	1
655	0.67±0.35	20.75±1.10	-0.999	18.36±0.00	2	0.72±0.07	20.94±0.23	-1.000	18.30±0.00	4.7	2
670	0.39±0.35	19.36±1.10	-0.999	18.37±0.00	1	0.36±0.05	19.24±0.15	-1.000	18.43±0.00	3.2	1
677	0.81±0.35	20.98±1.10	-0.999	17.89±0.00	1	0.92±0.08	21.38±0.29	-1.000	17.76±0.00	5.2	1
690	0.76±0.34	19.88±1.10	-0.999	17.07±0.00	2	0.67±0.01	19.60±0.03	-0.999	17.23±0.00	2.0	1
698	0.43±0.35	20.34±1.10	-0.998	19.19±0.00	2	0.37±0.06	20.19±0.14	-0.999	19.31±0.00	2.0	2
717	0.33±0.35	19.29±1.10	-0.998	18.61±0.00	2	0.33±0.13	19.33±0.39	-1.000	18.64±0.00	3.1	1
723	0.51±0.35	19.95±1.10	-0.999	18.38±0.00	2	0.48±0.05	19.85±0.15	-1.000	18.44±0.00	3.0	1
724	0.44±0.35	20.41±1.10	-0.998	19.17±0.00	3	0.51±0.12	20.67±0.39	-1.000	19.10±0.00	4.1	3
726	0.63±0.35	19.90±1.10	-0.999	17.73±0.00	1	0.65±0.06	20.01±0.20	-1.000	17.70±0.00	4.0	2
753	0.83±0.34	19.85±1.10	-0.999	16.68±0.00	1	0.81±0.03	19.79±0.08	-1.000	16.70±0.00	3.8	1
755	0.33±0.37	20.86±1.13	-0.993	20.16±0.00	2	0.29±0.35	20.72±1.02	-1.000	20.24±0.00	2.8	1
756	0.95±0.34	20.61±1.10	-0.999	16.81±0.00	2	1.19±0.05	21.53±0.18	-1.000	16.53±0.00	6.5	2
814	0.72±0.35	20.52±1.10	-0.999	17.89±0.00	2	0.58±0.04	20.04±0.11	-1.000	18.09±0.00	2.3	2
816	0.29±0.35	19.75±1.10	-0.998	19.27±0.00	1	0.27±0.13	19.69±0.39	-1.000	19.33±0.00	2.9	1
848	0.41±0.35	19.64±1.10	-0.998	18.55±0.00	1	0.40±0.16	19.59±0.51	-1.000	18.58±0.00	3.4	1
852	0.19±0.35	19.45±1.10	-0.998	19.46±0.00	2	0.18±0.22	19.43±0.57	-1.000	19.52±0.00	2.6	2
874	0.60±0.35	19.94±1.10	-0.999	17.92±0.00	1	0.56±0.05	19.80±0.15	-1.000	17.98±0.00	3.2	1
883	0.81±0.35	21.18±1.10	-0.999	18.10±0.00	2	0.63±0.03	20.59±0.07	-0.999	18.42±0.00	1.2	2
906	0.46±0.35	20.71±1.10	-0.998	19.39±0.00	2	0.39±0.20	20.55±0.46	-1.000	19.55±0.00	1.5	2

generates a best-fit template in parallel to fitting the kinematics.

Usually, both the stellar library and the galaxy spectra have spectral profiles closely approximating a Gaussian and so convolving with another Gaussian completes the process of matching the spectral resolutions. However, in the case of

GMOS the spectral profile is not Gaussian; thus matching the spectral profiles was somewhat involved and we dedicate an Appendix (B) to explaining our technique.

To calculate the recession velocities V and velocity dispersions σ of the individual galaxies, we made use of the freely available PPXF (penalised pixel fitting) IDL soft-

Mask	Exp. Times	Num of Frames.	Total exposure time	Dates of exposures	Notes
03	2400	6	14400	10/01/2002, 11/01/2002,	Light clouds on two exposures taken on 10th
04	2400,2580	4	10800	13/01/2002	
05	2400,3000	4	9960	12/01/2002	
06	2400,2100,3000	6	15000	14/01/2002, 15/01/2002	Guiding lost on last 10mins of one exposure

Table 5. Details of the GMOS/Gemini ground based spectra of the galaxies in Abell 1689.
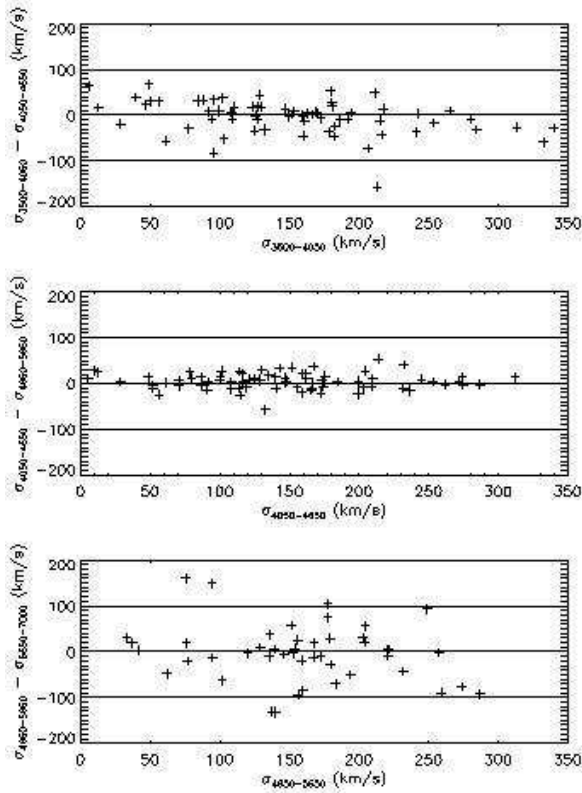
Figure 4. A comparison of the velocity dispersions σ derived from different wavelength ranges: $3500 < \lambda(\text{Å}) < 4050$, $4050 < \lambda(\text{Å}) < 4650$, $4650 < \lambda(\text{Å}) < 5650$ and $5650 < \lambda(\text{Å}) < 7000$.

ware (Cappellari & Emsellem 2004) to fit the parameterised stellar kinematics, and the GANDALF (Gas AND Absorption Line Fitting) IDL software (Sarzi et al. 2006) to fit any emission lines. We divided each input spectrum in four parts and fit them separately: wavelengths less than 4050 Å; between 4050 Å and 4650 Å; between 4650 Å and 5650 Å, and wavelengths greater than 5650 Å (all wavelengths quoted in the rest frame of the cluster). We also excluded regions affected by telluric absorption from the fit, such as the range $6850 < \lambda(\text{Å}) < 6950$. For each wavelength range a new best-fit stellar template was found. Fig. 4 shows the dispersions calculated from the middle two sections (4050 Å – 4650 Å and 4650 Å – 5650 Å) have the least scatter; thus we average the dispersions from these two regions for all subsequent analysis.

Although PPXF can determine dispersions less than the instrumental resolution (≈ 75 km s^{-1} at 0.5 μm), the errors (both random and systematic) increase. Consequently, we decided that dispersions found to be less than 50 km s^{-1}

are unreliable and we replace them with an upper limit of 50 km s^{-1} and do not use them to fit the scaling relations (see §3). This affects only 4/77 of galaxies, two of which could enter the KR and FJR as they have good HST surface photometry (#883 & #906).

We corrected our velocity dispersion measurements for aperture effects. Each spectrum was extracted from a rectangular aperture of size $1\rlap{.}''4$ by $1\rlap{.}''0$ and corrected to the equivalent circular radius following the procedure in Jørgensen et al. (1995b). We also correct our aperture dispersion measurements σ_{ap} to a velocity dispersion measured within a standard aperture size (1.62 kpc, equivalent $3\rlap{.}''4$ at the distance of Coma, Jørgensen et al. 1995b). The relation in Jørgensen et al. (1995b) is slightly different to the one found by Cappellari et al. (2006); however, the effect of this difference on our aperture corrections is small and we persist with the Jørgensen et al. relation for comparison with the literature.

2.7 The local comparison sample

To draw conclusions about the changes in the properties of the galaxies in Abell 1689 (at z=0.183), we need to compare them with local ($z \approx 0$) galaxies. For a fair comparison, we must select the local galaxies from a similar environment to the Abell 1689 galaxies (i.e. from a massive cluster) and the only suitably dense nearby environment is the Coma cluster ($z = 0.024$, Han & Mould 1992) at a distance of 103 ± 10Mpc (Liu & Graham 2001, Thomsen et al. 1997 but see also Jensen et al. 1999).

Fortunately, the ETGs in the Coma cluster have been rigorously investigated in the past. Like previous authors (Ziegler et al. 2001; La Barbera et al. 2003; Barr et al. 2005), we start with the data from Jørgensen et al. (1999a, hereafter J99): a total of 116 velocity dispersions for galaxies in Coma were compiled from the literature and homogenised in this work. We then compare the sample with the photometry of Jørgensen et al. (1995a, hereafter J95a) and find that all but 2 galaxies have Gunn r surface photometry available (calculated by fitting de Vaucouleurs curve-of-growth models). We adopt the formal uncertainties given in J95a and J99 but refrain from imposing covariances. Furthermore, we do not attempt to update the Galactic extinction, K-corrections or cosmological corrections but use the data as presented and model them (§4) as though they were observed at $z = 0.0$. We determine that this sample is 50% complete to r' $= 14.8$ (equivalent to $M_{r'} = -20.28$,see §C2).

Table 6. The kinematics of the spectroscopic sample within ± 6000km s^{-1} of z=0.183; out of 80 objects targeted, 3 were guide stars leaving 77 galaxies of which 71 were found to meet the criterion on $V_{\rm rec}$ to be considered part of the cluster. Those galaxies not in the cluster (and not shown here) were #160, #457, #892, #932, #983 and #1051; of these only #932 has $V_{\rm rec}$ relative to z=0.183 which could be in the cluster (8822km s^{-1}). However, none of these galaxies are found to be in the RS according to the mixture model (see Table 3). Velocity dispersions measured to be < 50km s^{-1} were deemed unreliable (well below the resolution of the instrument) and replaced with an upper limit of 50km s^{-1}; these points are not used when fitting the scaling relations, but are shown (as diamonds) in Fig. 6. Velocity dispersions given here have not been aperture corrected (see §2.6). *The full table appears in the online version.*

Spec. ID	$V_{\rm rec}$ (km s^{-1})	$\sigma_{\rm ap}$ (km s^{-1})
14	1672.2±2.4	83.2±3.5
15	-981.8±3.3	198.4±3.7
30	1638.8±2.0	125.0±2.5
45	300.8±4.0	104.3±5.4
70	1439.5±2.7	134.8±3.3
74	2524.8±3.5	159.1±4.2
91	2897.4±5.2	114.8±6.6
135	948.2±2.8	85.8±4.2
152	1291.9±2.9	158.2±3.4
217	299.5±2.9	172.6±3.3
218	2266.3±9.3	108.6±12.3
237	-934.2±4.2	170.8±4.8
239	1545.2±6.3	146.8±7.6
259	1284.4±2.3	73.6±3.7
286	2255.1±2.5	150.7±2.9
323	-83.9±2.9	90.3±4.4
341	802.2±5.1	201.6±5.5
343	-1257.0±4.3	215.3±4.7
...	...	...

2.7.1 Comparing Coma and Abell 1689

We wish to infer ages and formation timescales of the ETGs in Abell 1689 and Coma by assuming that galaxies in Abell 1689 will evolve into those in Coma over 2.26 Gyr. This assumption is not immediately obvious; furthermore, if untrue it could invalidate our analysis. In a hierarchical picture, one expects more massive DM halos to collapse earlier and potentially produce galaxies earlier; thus, if Abell 1689 were considerably more massive than Coma was at z=0.183, it is not unreasonable to claim that the Abell 1689 population would be older, leading to a smaller CMR scatter and $\Delta\beta$, thus biasing our measurements. We now look at these two clusters in detail and discuss how similar or different they are. We address the X-ray luminosities, the cluster masses and the known details of the galaxy populations to gauge how robust our approach is.

While Coma is relatively X-ray bright ($L_X = 7.21 \times 10^{44}$ erg s^{-1}), its luminosity somewhat dwarfed by the (exceptionally) high X-ray luminosity of Abell 1689 ($L_X = 20.74 \times 10^{44}$ erg s^{-1}). On X-ray luminosity evidence alone, one might conclude that the mass of Abell 1689 is many times the mass of Coma, or that Abell 1689 has recently undergone a merger (it hasn't, according to the relaxed nature of the X-ray contours, Lemze et al.

2008). However, the X-ray luminosity is only part of the picture; indeed, detailed X-ray modelling of Coma and Abell 1689 indicate that their total masses are quite comparable given the modelling uncertainties (around 5×10^{14} M$_\odot$: Mason & Myers 2000; Ettori et al. 2002; Peng et al. 2009; Riemer-Sørensen et al. 2009; Mahdavi et al. 2008). The lensing view on the two cluster masses is broadly similar: although Abell 1689 appears marginally more massive than Coma, there is considerable scatter in the lensing estimates (mass estimates for both are around $1 - 2 \times 10^{15}$ M$_\odot$: Kubo et al. 2007; Gavazzi et al. 2009; Okabe et al. 2010; Broadhurst et al. 2005; Halkola et al. 2006; Mahdavi et al. 2008).

We note (like many others) that the X-ray masses of the inner regions of clusters are generally estimated to be half those of the lensing measurements. Oguri et al. (2005) and Morandi et al. (2011) were able to resolve this discrepancy with triaxial halos and suggest Abell 1689 is viewed along its major axis. This is unlikely for Coma as we see the two central BCGs well separated on the sky. Thus certain discrepancies between Coma and Abell 1689 could in part be down to projection effects.

In terms of mass evolution, it is unlikely that Abell 1689 will become much more massive between z=0.183 and now: according to the work of Fakhouri et al. (2010), for halo masses $> 10^{14}$M$_\odot$, the rate of change of mass at $0 < z < 0.2$ is $< 4 \times 10^4$M$_\odot$yr^{-1}: therefore, the expected increase in mass over 2.26 Gyr is $< 9.2 \times 10^{13}$M$_\odot$, which is a small fraction of the total mass.

Thus we conclude that, aside from projection effects from possible triaxiallity, the two clusters are well matched in mass and are both reasonably relaxed.

2.8 Magnitude conversions, Cosmological corrections and evolution measurements

We cannot compare the Coma data to the Abell 1689 data directly: the data are in different filter bands using different magnitude systems. Furthermore, the Abell 1689 data are affected by cosmological dimming (the Coma data has been corrected for this, see §2.7) and evolution of the stellar population (the magnitude of which we wish to determine). Therefore, we must address these differences and where appropriate apply corrections or model the effects (see §4).

2.8.1 Magnitude systems

The Coma data of JF95a was observed in the Gunn r-band using the Gunn photometric system (relative to a subdwarf F6 star) whereas the HST F625W observations are in the AB system. We convert the Gunn r photometry to the AB system using the corrections listed in Frei & Gunn (1994).

2.8.2 Cosmological Corrections

When we observe galaxies at significant redshifts, it is necessary to correct for cosmological effects (i.e. expansion and redshift). We adopt the approaches described in Hogg (1999) and Hogg et al. (2002) to correct our measurements. We split the K-correction (Hogg et al. 2002) into two terms,

$$K = K_b + K_c. \tag{12}$$

The bandpass term K_b is easily corrected in the AB magnitude system by *reducing* the observed brightness by $(1+z)$. However, the colour term K_c depends on the details of the underlying stellar population which change with age, metallicity, initial mass function (IMF), dust content, etc.. J95a assumed no *evolution* of the galaxy SED when calculating the colour term of the K-correction K_c for the Coma data, which is a good approximation at low redshift. But at higher redshifts, we do not know the exact SED so we do not apply a K_c correction to our measurements of Abell 1689. In §4, we describe how we model our observations by calculating magnitudes based on stellar population models in blueshifted filter profiles, thus negating the need for K_c. However, it is necessary to correct for *Tolman* dimming (Tolman 1930; Lubin & Sandage 2001). Incorporating this and K_b, the bandpass limited AB surface brightness μ_{obs} is related to the bandpass limited rest-frame AB surface brightness μ_{rest} by

$$\mu_{\mathrm{rest}} = \mu_{\mathrm{obs}} + 7.5\log(1+z). \qquad (13)$$

Furthermore, we can calculate apparent magnitudes using

$$m = \langle\mu\rangle_{\mathrm{e,rest}} - 5\log(R_e) - 2.5\log(2\pi) + 7.5\log(1+z) \quad (14)$$

and (bandpass corrected) absolute magnitudes using

$$\mathcal{M} = m + 2.5\log(1+z) - 5\log(D_L) + 5 \qquad (15)$$

where R_e is measured in arcseconds and D_L is the luminosity distance in pc.

2.8.3 Size evolution

Recent literature suggests that galaxies (both disks and spheroids) were more compact in the past (Mo et al. 1998; Ferguson et al. 2004; Bouwens et al. 2004; Trujillo et al. 2007; van der Wel et al. 2008; Hopkins et al. 2009). The details are still very much a topic of debate: the degree of compactness could depend on galaxy mass (Barden et al. 2005; McIntosh et al. 2005; Trujillo et al. 2007). We measure R_e, $\langle\mu\rangle_e$ and σ (for Coma and Abell 1689) with and without correcting size evolution. The corrections we apply assume that the effective radius now, R_e, is related to the effective radius at non-zero redshift, $R_{e,z}$, by a simple power-law scaling,

$$\log(R_e) = \log(R_{e,z}) + \zeta\log(1+z) \qquad (16)$$

and therefore, assuming no other changes,

$$\langle\mu\rangle_e = \langle\mu\rangle_{e,z} + 5\zeta\log(1+z). \qquad (17)$$

The value of ζ is still debated: for massive, high concentration galaxies, Bouwens et al. (2004) find $\zeta = 1.05\pm0.21$ over the range $2.5 < z < 6$ which agrees with van der Wel et al. (2008) who found $\zeta = 0.98\pm0.11$ between $0 < z < 1$ for morphologically selected ETGs. However, Trujillo et al. (2007) found slightly stronger evolution for massive spheroid-like (highly concentrated) galaxies: a factor of 4 ± 0.4 since $z = 1.5$, equivalent to $\zeta = 1.6$. We adopt a value $\zeta = 1.0$ in this work.

We also calculate the equivalent velocity dispersion now, σ, from the velocity dispersion measured at higher redshift, σ_z, to be

$$\log(\sigma) = \log(\sigma_z) - 0.5\eta\log(1+z). \qquad (18)$$

with $\eta = 1.0$. In dynamical models of Sérsic-like galaxies, the projected line-of-sight velocity dispersion changes in this way when R_e is scaled, if the Sérsic index is unchanged Ciotti (1991). However, Hopkins et al. (2010) suggest the Sérsic index *does* change. The effect of size evolution on the velocity dispersion is difficult to measure and not well constrained (van der Wel et al. 2008; Cappellari et al. 2009; van Dokkum et al. 2009; Hopkins et al. 2010). Cenarro & Trujillo (2009) report a value of $\eta \approx 0.6$ while the single observation by van Dokkum et al. (2009) would suggest $\eta \approx 2$. In the absence of a clear measurement of the change in the Sérsic index, we adopt $\eta = 1.0$.

2.9 Fitting 2D scaling relations

There are many different techniques available to fit (thereby represent) scaling relations. The disadvantages and limitations of common techniques are discussed by Hogg et al. (2010) who advocate Markov Chain Monte Carlo (MCMC) methods. We follow these guidelines and use MCMC methods to *explore the posterior distributions of the parameters in each assumed model*; details are given in Appendix C. We investigate three different models: one where the data (with uncertainties) are drawn from a linear relation with unknown slope, intercept and intrinsic dispersion and we do not attempt to correct for magnitude cuts or selection effects (hereafter the linear model or LM); a double linear model where two sets of data (with uncertainties) are assumed to have the same slope and intrinsic dispersion but with different intercepts and we apply corrections for magnitude cuts and selection effects (hereafter the double linear model or DLM); and finally, a model where the data are drawn from a mixture of two distributions: one being the linear model as before, and another *outlier* distribution having unknown first and second moments (hereafter the mixture model, or MM). In all cases, we assume normal distributions for the models.

We use the LM and DLM to fit the KRs and FJRs of Coma and Abell 1689 to measure any offset (i.e. evolution) between them. We use the MM to isolate and measure the intrinsic scatter of the CMR in Abell 1689.

3 RESULTS AND ANALYSIS

We present the Faber-Jackson relation, the Kormendy relation and the colour magnitude diagram for Abell 1689, below. As discussed in §1.3, we will present and analyse the FP in a future paper.

3.1 g'- r' Colour Magnitude Diagram

The raw g'-r' colour magnitude diagram (CMD) for Abell 1689 was presented earlier in Fig. 3, showing only the data where the uncertainties were less than 0.1 mag. The RS is clearly visible, along with a blue cloud. We also over plot (dotted lines) the selection limits for the GMOS-N spectroscopic sample and show as an insert the luminosity distribution of the parent sample and the spectroscopic sample.
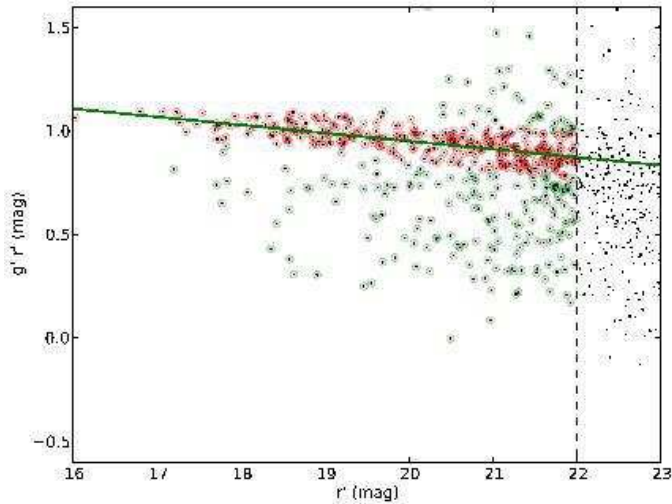
Figure 5. CMD with RS shown (red) and outliers (green) rejected by the MCMC mixture model.

3.1.1   Measured scatter of the CMR in Abell 1689

We use a mixture model (see §2.9 & Appendix C) to measure the slope, intercept and intrinsic scatter of the CMR (Eq. 4). We restrict the galaxies in the sample to be brighter than $r' < 22$ mag as well as the constraints described §2.3. We do not apply constraints on the recession velocities or morphologies of the galaxies, which can only increase the measured scatter.

The results of fitting the MCMC mixture model are given in Table 7; in particular, the intrinsic scatter is found to be $\sigma_{\mathrm{CMR}} = 0.054 \pm 0.004$ mag.

In Fig. 5 we show the CMD of Abell 1689 with the galaxies marked according to which of the two distributions they were most likely to be members of. We also show the best fit to the CMR, marginalised over all other parameters. There is an excess of galaxies below the RS, and a few above, which are considered to be *outliers* by the mixture model (points highlighted in green), but the mixture model has successfully isolated the RS (points highlighted in red) *without any cut in colour or clipping* imposed *a priori*. The limit in magnitude ($r' < 22$ mag) affects the resulting scatter significantly: brighter (lower) magnitude cuts decrease the scatter while fainter (higher) magnitude cuts increase the scatter. Magnitudes are taken from the entire GMOS r-band image, with dimensions $280'' \times 300''$.

BKT98 quote Coma's CMR scatter inside $R < 600$ kpc to be 0.049 for all galaxies brighter than $\mathcal{M}_V < -18.2$ mag (98 galaxies). We fit the CMR to galaxies brighter than $\mathcal{M}_V < -17.90$ mag inside $R < 570$ kpc. The selection effects and resulting scatter in both clusters is very similar; the scatter in Coma is slightly smaller though uncertainties are not given by BKT98. More recently, Terlevich et al. (2001) performed a more extensive study of the CMR in Coma: for all galaxies brighter than $\mathcal{M}_V < -18.2$ mag in roughly a square degree (175 galaxies), they quote an intrinsic scatter of $0.063 \pm^{0.008}_{0.01}$ mag, which is statistically consistent with our result for Abell 1689 (although our uncertainties are a factor of 2 smaller).

We highlight a handful of objects at relatively faint magnitudes ($r' \sim 21$ mag) that lie above the CMR. These ex-

cessively red objects are found beyond $r' > 20$ mag, so they do not enter our spectroscopic sample. Galaxies redder than the RS could be excessively old, excessively metal rich, heavily extincted and/or intermediate or high redshift interlopers. Alternatively, we could be underestimating the scatter in the CMR at this magnitude (particularly because we assume a single scatter across all magnitudes). Terlevich et al. (1999) correlated the residuals of the CMR with spectral absorption line indices and showed that the galaxies scattered *blueward* of the mean relation have an increased hydrogen Balmer absorption and are thus younger: if the reverse is true, galaxies redder than the RS could be old relics from the initial cluster population. It is also worth noting that for ages approaching 14Gyr and metallicities around twice solar, both the BC03 and M05 models predict a maximum g'-r' colour of $\lesssim 1.4$. Thus the few objects redder than g'-r' $=1.4$ are unlikely to be part of the cluster unless they are extremely metal rich or extincted; conversely, the majority of the red objects that have g'-$r' < 1.4$ but are redder than the RS could be cluster members, in principle.

3.2   The Faber-Jackson relation

Table 7 presents the results for fits to the FJRs (Eq. 1) of Coma and Abell 1689 using individual linear models (LMs) and the double linear model (DLM).

In Abell 1689, the calculation of the surface photometry for the central BCGs (brightest cluster or cD galaxies: #584 & #610) was compromised by contamination from other galaxies and the ICL. Similar arguments could be made for the two BCGs in Coma (GMP2921 & GMP3329). Thus we fit the data both with and without the two BCGs and with and without correcting for size evolution (see §2.8.3).

The values for $\Delta\beta_{\mathrm{FJR}}$ in Table 7 were either calculated by subtracting the absolute magnitude of the FJR at $\log\sigma = 2.2$ (where the FJRs are best constrained in individual LMs) or directly when fitting the DLM to both the Abell 1689 and Coma data. For nearly all cases, the galaxies in Abell 1689 are fainter in the F625W band than the Coma galaxies in the r'-band. The evolution measured from the LMs and DLM generally agree, suggesting little bias from cuts or selection effects in the FJR.

Correcting for size evolution has a significant effect in decreasing the measured evolution between Abell 1689 and Coma, decreasing $\Delta\beta$ by around 0.25 mag; removing the BCGs increases $\Delta\beta$ by around 0.05 mag.

Fig. 6 shows the FJR measured for Abell 1689 in F625W compared to that measured for Coma in the r'-band. Both de Vaucouleurs and Sérsic surface photometry are shown for Abell 1689 but only de Vaucouleurs photometry is available for Coma. We have corrected the data points for size evolution and over plot the best fit DLM (omitting BCGs) in each case. The DLM fits the data well and both the Coma and Abell 1689 galaxies populate the same $\{m, \sigma\}$ parameter space.

3.3   Kormendy relation

Table 7 presents the results for the fits to the KRs (Eq. 2) of Coma and Abell 1689 using LMs and the DLM, as was done for the FJR above.

Colour-Magnitude Relation: $(g'-r') = \alpha_{\mathrm{CMR}}(r'-20) + \beta_{\mathrm{CMR}}$

α_{CMR}	β_{CMR}	σ_{CMR}	Model	Notes
-0.039±0.003	0.951±0.004	0.054±0.004	MM	Fit to sources with $r' < 22$.

Faber-Jackson Relation: $\mathcal{M} = \alpha_{\mathrm{FJR}}\log(\sigma) + \beta_{\mathrm{FJR}}$

α_{FJR}	β_{FJR}	$\sigma_{\mathrm{I}}(\mathrm{FJR})$	$\mathcal{M}(\log\sigma = 2.2)$	$\Delta\beta_{\mathrm{FJR}}$	Model	SEC	Cluster	Profile	Notes
$-8.67^{+0.77}_{-0.95}$	$-2.1^{+2.1}_{-1.7}$	$0.0917^{+0.0076}_{-0.0068}$	$-21.198^{+0.08}_{-0.082}$	-	LM	N	Coma	dV	all galaxies
$-10.6^{+2}_{-3.1}$	$2.6^{+7.1}_{-4.5}$	$0.106^{+0.017}_{-0.015}$	$-20.70^{+0.28}_{-0.22}$	$0.50^{+0.29}_{-0.24}$	LM	N	Abell 1689	dV	all galaxies
$-10.0^{+1.8}_{-2.7}$	$1.2^{+6.1}_{-4.1}$	$0.109^{+0.016}_{-0.013}$	$-20.69^{+0.26}_{-0.21}$	$0.51^{+0.27}_{-0.22}$	LM	N	Abell 1689	S	all galaxies
$-8.73^{+0.59}_{-0.73}$	$-1.6^{+1.6}_{-1.3}$	$0.0938^{+0.006}_{-0.0055}$	-	$0.42^{+0.14}_{-0.13}$	DLM	N	Both	dV	all galaxies
$-8.93^{+0.58}_{-0.72}$	$-1.1^{+1.6}_{-1.3}$	$0.0980^{+0.0056}_{-0.0051}$	-	$0.46^{+0.13}_{-0.12}$	DLM	N	Both	dV+S	all galaxies
$-8.32^{+0.8}_{-1.02}$	$-2.9^{+2.2}_{-1.8}$	$0.0911^{+0.0077}_{-0.007}$	$-21.186^{+0.079}_{-0.08}$	-	LM	N	Coma	dV	no BCGs
$-7.6^{+1.2}_{-1.7}$	$-3.9^{+3.7}_{-2.6}$	$0.081^{+0.018}_{-0.018}$	$-20.73^{+0.17}_{-0.15}$	$0.45^{+0.19}_{-0.17}$	LM	N	Abell 1689	dV	no BCGs
$-7.9^{+1.2}_{-1.6}$	$-3.4^{+3.7}_{-2.7}$	$0.094^{+0.016}_{-0.013}$	$-20.69^{+0.18}_{-0.15}$	$0.49^{+0.2}_{-0.17}$	LM	N	Abell 1689	S	no BCGs
$-7.92^{+0.52}_{-0.58}$	**$-3.3^{+1.3}_{-1.2}$**	**$0.0866^{+0.0057}_{-0.0055}$**	**-**	**$0.44^{+0.12}_{-0.12}$**	**DLM**	**N**	**Both**	**dV**	**no BCGs**
$-8.10^{+0.55}_{-0.66}$	**$-2.9^{+1.5}_{-1.2}$**	**$0.0906^{+0.0054}_{-0.0051}$**	**-**	**$0.50^{+0.11}_{-0.1}$**	**DLM**	**N**	**Both**	**dV+S**	**no BCGs**
$-8.69^{+0.79}_{-0.93}$	$-2.1^{+2}_{-1.7}$	$0.0918^{+0.0076}_{-0.0069}$	$-21.243^{+0.08}_{-0.083}$	-	LM	Y	Coma	dV	all galaxies
$-10.6^{+2}_{-3.1}$	$2.3^{+6.9}_{-4.4}$	$0.106^{+0.018}_{-0.015}$	$-21.09^{+0.23}_{-0.21}$	$0.15^{+0.24}_{-0.22}$	LM	Y	Abell 1689	dV	all galaxies
$-10.0^{+1.8}_{-2.7}$	$0.9^{+5.9}_{-4}$	$0.109^{+0.016}_{-0.014}$	$-21.04^{+0.21}_{-0.2}$	$0.20^{+0.22}_{-0.21}$	LM	Y	Abell 1689	S	all galaxies
$-8.65^{+0.55}_{-0.78}$	$-2.1^{+1.7}_{-1.2}$	$0.0937^{+0.0058}_{-0.0054}$	-	$0.14^{+0.12}_{-0.13}$	DLM	Y	Both	dV	all galaxies
$-8.97^{+0.67}_{-0.67}$	$-1.3^{+1.4}_{-1.5}$	$0.0980^{+0.0055}_{-0.005}$	-	$0.19^{+0.12}_{-0.13}$	DLM	Y	Both	dV+S	all galaxies
$-8.33^{+0.84}_{-1.02}$	$-2.9^{+2.2}_{-1.8}$	$0.0912^{+0.0078}_{-0.0069}$	$-21.230^{+0.08}_{-0.082}$	-	LM	Y	Coma	dV	no BCGs
$-7.6^{+1.2}_{-1.7}$	$-4.2^{+3.7}_{-2.7}$	$0.081^{+0.019}_{-0.018}$	$-21.01^{+0.14}_{-0.14}$	$0.22^{+0.16}_{-0.16}$	LM	Y	Abell 1689	dV	no BCGs
$-7.9^{+1.2}_{-1.6}$	$-3.7^{+3.6}_{-2.7}$	$0.094^{+0.015}_{-0.013}$	$-20.98^{+0.15}_{-0.14}$	$0.25^{+0.17}_{-0.16}$	LM	Y	Abell 1689	S	no BCGs
$-7.98^{+0.45}_{-0.67}$	**$-3.5^{+1.4}_{-1}$**	**$0.0868^{+0.0057}_{-0.0054}$**	**-**	**$0.19^{+0.11}_{-0.11}$**	**DLM**	**Y**	**Both**	**dV**	**no BCGs**
$-7.98^{+0.49}_{-0.61}$	**$-3.4^{+1.3}_{-1.1}$**	**$0.0905^{+0.0054}_{-0.0049}$**	**-**	**$0.25^{+0.11}_{-0.1}$**	**DLM**	**Y**	**Both**	**dV+S**	**no BCGs**

Kormendy Relation : $\langle\mu\rangle_e = \alpha_{\mathrm{KR}}\log(R_e) + \beta_{\mathrm{KR}}$

α_{KR}	β_{KR}	$\sigma_{\mathrm{I}}(\mathrm{KR})$	$\langle\mu\rangle_e(\log R_e = 0.5)$	$\Delta\beta_{\mathrm{KR}}$	Model	SEC	Cluster	Profile	Notes
$3.84^{+0.28}_{-0.24}$	$17.95^{+0.12}_{-0.13}$	$0.150^{+0.011}_{-0.01}$	$19.870^{+0.064}_{-0.061}$	-	LM	N	Coma	dV	all galaxies
$3.67^{+0.42}_{-0.26}$	$18.10^{+0.26}_{-0.36}$	$0.165^{+0.026}_{-0.025}$	$19.94^{+0.11}_{-0.12}$	$0.07^{+0.13}_{-0.14}$	LM	N	Abell 1689	dV	all galaxies
$3.99^{+0.63}_{-0.49}$	$17.94^{+0.3}_{-0.38}$	$0.168^{+0.024}_{-0.02}$	$19.93^{+0.12}_{-0.13}$	$0.06^{+0.14}_{-0.14}$	LM	N	Abell 1689	S	all galaxies
$4.11^{+0.22}_{-0.2}$	$18.06^{+0.12}_{-0.13}$	$0.1522^{+0.0089}_{-0.0085}$	-	$0.218^{+0.093}_{-0.095}$	DLM	N	Both	dV	all galaxies
$4.16^{+0.23}_{-0.21}$	$18.03^{+0.13}_{-0.14}$	$0.1579^{+0.0084}_{-0.0077}$	-	$0.211^{+0.095}_{-0.098}$	DLM	N	Both	dV+S	all galaxies
$4.22^{+0.31}_{-0.27}$	$17.83^{+0.12}_{-0.14}$	$0.1319^{+0.0104}_{-0.0091}$	$19.942^{+0.065}_{-0.061}$	-	LM	N	Coma	dV	no BCGs
$4.67^{+0.76}_{-0.69}$	$17.63^{+0.38}_{-0.42}$	$0.106^{+0.04}_{-0.059}$	$19.97^{+0.13}_{-0.13}$	$0.03^{+0.14}_{-0.14}$	LM	N	Abell 1689	dV	no BCGs
$4.29^{+0.66}_{-0.51}$	$17.83^{+0.31}_{-0.39}$	$0.150^{+0.023}_{-0.019}$	$19.98^{+0.12}_{-0.12}$	$0.04^{+0.14}_{-0.14}$	LM	N	Abell 1689	S	no BCGs
$4.39^{+0.21}_{-0.19}$	**$17.96^{+0.12}_{-0.12}$**	**$0.1313^{+0.0085}_{-0.0079}$**	**-**	**$0.199^{+0.091}_{-0.094}$**	**DLM**	**N**	**Both**	**dV**	**no BCGs**
$4.41^{+0.22}_{-0.21}$	**$17.93^{+0.13}_{-0.14}$**	**$0.1424^{+0.0077}_{-0.0072}$**	**-**	**$0.173^{+0.094}_{-0.095}$**	**DLM**	**N**	**Both**	**dV+S**	**no BCGs**
$3.84^{+0.28}_{-0.25}$	$17.96^{+0.12}_{-0.13}$	$0.150^{+0.011}_{-0.01}$	$19.881^{+0.063}_{-0.06}$	-	LM	Y	Coma	dV	all galaxies
$3.66^{+0.59}_{-0.41}$	$18.20^{+0.28}_{-0.39}$	$0.165^{+0.024}_{-0.024}$	$20.03^{+0.12}_{-0.14}$	$0.15^{+0.14}_{-0.15}$	LM	Y	Abell 1689	dV	all galaxies
$3.98^{+0.64}_{-0.49}$	$18.01^{+0.34}_{-0.43}$	$0.168^{+0.023}_{-0.02}$	$20.00^{+0.13}_{-0.15}$	$0.12^{+0.15}_{-0.17}$	LM	Y	Abell 1689	S	all galaxies
$4.11^{+0.21}_{-0.2}$	$18.13^{+0.13}_{-0.14}$	$0.1524^{+0.009}_{-0.0085}$	-	$0.276^{+0.096}_{-0.1}$	DLM	Y	Both	dV	all galaxies
$4.09^{+0.22}_{-0.21}$	$18.13^{+0.14}_{-0.15}$	$0.1584^{+0.0084}_{-0.0078}$	-	$0.279^{+0.097}_{-0.103}$	DLM	Y	Both	dV+S	all galaxies
$4.23^{+0.31}_{-0.27}$	$17.84^{+0.12}_{-0.14}$	$0.1322^{+0.0101}_{-0.0091}$	$19.949^{+0.065}_{-0.061}$	-	LM	Y	Coma	dV	no BCGs
$4.68^{+0.78}_{-0.69}$	$17.65^{+0.43}_{-0.49}$	$0.107^{+0.04}_{-0.058}$	$20.00^{+0.14}_{-0.16}$	$0.05^{+0.15}_{-0.17}$	LM	Y	Abell 1689	dV	no BCGs
$4.30^{+0.66}_{-0.52}$	$17.88^{+0.34}_{-0.43}$	$0.150^{+0.023}_{-0.019}$	$20.03^{+0.13}_{-0.15}$	$0.08^{+0.15}_{-0.16}$	LM	Y	Abell 1689	S	no BCGs
$4.40^{+0.2}_{-0.2}$	**$18.00^{+0.13}_{-0.14}$**	**$0.1312^{+0.0085}_{-0.0079}$**	**-**	**$0.238^{+0.094}_{-0.098}$**	**DLM**	**Y**	**Both**	**dV**	**no BCGs**
$4.41^{+0.23}_{-0.21}$	**$17.97^{+0.15}_{-0.15}$**	**$0.1424^{+0.0078}_{-0.0075}$**	**-**	**$0.212^{+0.099}_{-0.103}$**	**DLM**	**Y**	**Both**	**dV+S**	**no BCGs**

Table 7. Parameters and marginalised uncertainties for the fits to the Faber-Jackson and Kormendy relations for Coma and Abell 1689 as well as the CMR relation for Abell 1689. Model abbreviations are: MM=Mixture model; LM=Linear model; DLM=Double linear model. The column headed SEC shows whether a size evolution correction was applied (§2.8.3). The Profile column shows if the surface photometry (COG) was calculated using de Vaucouleurs (dV) or Sérsic (S) profiles. Note that in the double linear fits made to Coma and Abell 1689 data, the Coma data is archival and was measured using de Vaucouleurs COGs while for the Abell 1689 data we had the option to fit Sérsic or de Vaucouleurs profiles. Where BCGs were removed from the fitting procedure, we removed galaxies #584 and #610 from the Abell 1689 sample and GMP2921 and GMP3329 from the Coma sample. For the KR and FJR, results in bold are the ones we consider to be most reliable: note that without size evolution corrections the FJR and KR luminosity evolutions disagree (2σ). Taking the average of (i.e. combining the samples for) the KR and FJR results corrected for size evolution while excluding BCGs gives $\Delta\beta = 0.22 \pm 0.11$ mag (see §3.5) which we compare to stellar population models in §4.2
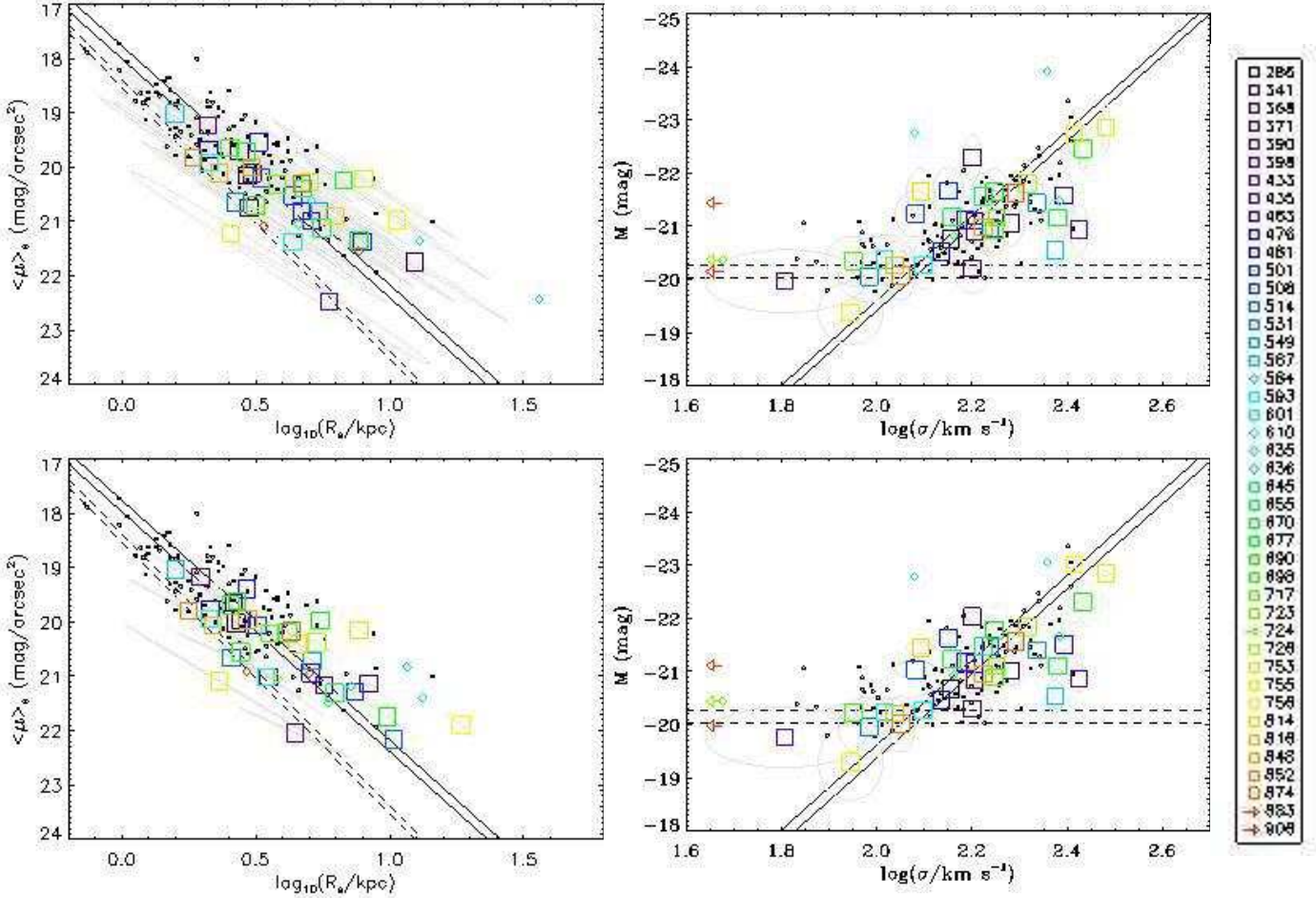
Figure 6. The de Vaucouleurs (top) and Sérsic (bottom) Kormendy (left) and Faber-Jackson (right) relations for Abell 1689. Squares represent good data while diamonds and arrows represent bad data (poor COG fits, or upper limits on velocity dispersions) that were excluded from the fits. Small black squares represent Coma data from Jørgensen et al. (1995a, in the r-band, corrected to the AB system) and Jørgensen et al. (1999b) while large coloured symbols represent data for Abell 1689 (from HST/ACS F625W imaging and GMOS-N spectroscopy). Error ellipses on the Abell 1689 data are shown in light grey and account for correlations between each axis. The error bars are larger for the de Vaucouleurs data because they include the systematic errors associated with fixing the Sérsic index to $n = 4$. Solid lines show the results of fitting the double linear models without BCGs: the light solid line represents the Coma data while the bold solid line represents the Abell 1689 data. Dashed lines illustrate the magnitude cuts (50% completeness) for the Abell 1689 sample (bold dashed) and the Coma sample (light dashed). Note that bad points (diamonds) may lie outside the plotting window. Galaxies for which $\sigma < 50$km s^{-1} are shown as upper limits in the FJR (#724, #884 & #906).

The values for $\Delta\beta_{\mathrm{KR}}$ in Table 7, like $\Delta\beta_{\mathrm{FJR}}$, were calculated both at $\log R_e = 0.5$ from individual LMs, and directly from the DLM. As before, we favour the values calculated by the DLM. As for the FJR, galaxies in Abell 1689 are fainter in the F625W band than Coma galaxies in the r'-band ($\Delta\beta > 0$). Unlike the FJR, there is a significant difference between the evolution measured from the LMs and the DLM: the KR is sensitive to magnitude cuts and selection effects which is unsurprising given that the cut runs almost parallel to the KR (unlike the FJR). Correcting for size evolution increases $\Delta\beta_{\mathrm{KR}}$ only by around 0.05 mag, while including the BCGs has a negligible effect: clearly the KR is relatively robust to these two factors.

Fig. 6 shows the KR measured for Abell 1689 in F625W compared to that measured for Coma in the r'-band. Both de Vaucouleurs and Sérsic surface photometry are shown (for Abell 1689) and as before, we have corrected the data for size evolution and over plot the best fit DLM (omit-

ting BCGs). The galaxies in Abell 1689 *do not* populate the same $\{\langle\mu\rangle_e, R_e\}$ parameter space as the Coma galaxies: there appear to be more bright, compact galaxies in Coma. Recall that we have corrected the Abell 1689 galaxies for size evolution, thus making them larger and fainter, but we did not apply any cuts in R_e or $\langle\mu\rangle_e$ *a priori*; the only cut was in absolute magnitude, which is well matched to the absolute magnitude cut in the Coma sample. Indeed, using SEXTRACTOR effective radii as an estimate for size, there is no difference between the size distributions of our spectroscopic sample and the parent sample with r' < 19.5. Thus the different locations of the Coma and Abell 1689 data along the KR are not due to size selection effects.

3.4 The effects of size evolution in the KR and FJR

Without correction for size evolution and excluding BCGs, the measured $\Delta\beta_{\mathrm{KR}}$ and $\Delta\beta_{\mathrm{FJR}}$ disagree at the 2σ level. Although the need to correct for size evolution is at a modest statistical significance, reviewing the effect reveals why the FJR was more affected than the KR.

If we consider both the corrections to R_e and $\langle\mu\rangle_e$, using our knowledge of how these two are related (Eq. 2) we can infer how they shift the whole relation up or down in $\langle\mu\rangle_e$, which can be (mistakenly) interpreted as luminosity evolution of the stellar population. Using Eq. 16 and Eq. 17 in Eq. 2, we find

$$\mu_{e,z} = \alpha_{\mathrm{KR}}\log R_{e,z} + \beta_{\mathrm{KR}} + \Delta\beta'_{\mathrm{KR}} \qquad (19)$$

with

$$\Delta\beta'_{\mathrm{KR}} = (\alpha_{\mathrm{KR}} - 5)\zeta\log(1 + z). \qquad (20)$$

This $\Delta\beta'_{\mathrm{KR}}$ appears as a change in the surface brightness; it arises just from scaling the size of the galaxies and not from changes in the stellar populations. We see that the effects from changing R_e and $\langle\mu\rangle_e$ counteract with each other in the KR: the typical value for α_{KR} is ~ 4, which with $\zeta = 1$, gives $\Delta\beta'_{\mathrm{KR}} = -\log(1 + z)$. This tells us that if we were to compare $\langle\mu\rangle_e$ vs. $\log R_e$ for Coma to $\langle\mu\rangle_{e,z}$ vs. $\log R_{e,z}$ for Abell 1689, even without any changes in the stellar populations, we would find that the Abell 1689 galaxies appear *brighter* than the standard KR prediction by $\log(1 + z)$.

Repeating this analysis for the FJR relation using Eq. 18 in Eq. 1, we find a similar relation to before

$$\mathcal{M} = \alpha_{\mathrm{FJR}}\log(\sigma_z) + \beta_{\mathrm{FJR}} + \Delta\beta'_{\mathrm{FJR}} \qquad (21)$$

but this time with

$$\Delta\beta'_{\mathrm{FJR}} = -0.5\alpha_{\mathrm{FJR}}\eta\log(1 + z). \qquad (22)$$

As with the KR, one could easily misinterpret $\Delta\beta'_{\mathrm{FJR}}$ as luminosity evolution of the stellar populations, but it is in fact just an effect of size evolution. However, unlike the KR, the change is quite substantial. Our typical α_{FJR} is ~ -8 and with $\eta = 1$, gives $\Delta\mathcal{M} = 4\log(1 + z)$. If we were to compare $\mathcal{M}$ vs. $\log\sigma$ for Coma to $\mathcal{M}_z$ vs. $\log\sigma_z$ for Abell 1689 and there was no change to the stellar populations, we would still find Abell 1689 galaxies to be *fainter* than the standard FJR prediction by $4\log(1 + z)$. The canonical value for α_{FJR} is ~ 10 ($L \sim \sigma^4$), which increases the effect to $5\log(1 + z)$.

Thus size evolution has opposite effects in the KR and the FJR: it makes the KR of earlier galaxy populations appear *brighter*, the FJR *fainter*, and we observe these changes in $\Delta\beta_{\mathrm{FJR}}$ and $\Delta\beta_{\mathrm{KR}}$.

3.5 Luminosity evolution from the KR and FJR

After correcting for size evolution, the differences between the KRs and FJRs of Coma and Abell 1689 ($\Delta\beta_{\mathrm{KR}}$ and $\Delta\beta_{\mathrm{FJR}}$) agree. To avoid propagating multiple calculations of $\Delta\beta$ any further, we now consider which values are our best estimates.

The values of $\Delta\beta$ calculated using the DLM account for magnitude cuts and selection effects and are fully marginalised over the other model parameters; the values calculated from separate LMs to Coma and Abell 1689 are

only marginalised over the model parameters fitted to each cluster, depend on where (on the x-axis) we compare the two clusters, and do not account for magnitude cuts or selection effects. We favour calculating $\Delta\beta$ using the DLM for these reasons. However, the DLM, as currently defined, cannot address downsizing.

We should only consider values of $\Delta\beta$ which were calculated with size evolution corrections: without such corrections, $\Delta\beta_{\mathrm{KR}}$ and $\Delta\beta_{\mathrm{FJR}}$ disagree. Including BCGs reduces $\Delta\beta_{\mathrm{FJR}}$ and has a negligible effect on $\Delta\beta_{\mathrm{KR}}$, but the changes are small and within the uncertainties. The average $\Delta\beta$ *with* BCGs is 0.23 mag while the average without BCGs is 0.22 mag. We somewhat arbitrarily choose to use the values of $\Delta\beta$ calculated without the BCGs (see §5.3). Finally, $\Delta\beta$ measured using Sérsic photometry in Abell 1689 is on average slightly larger than that measured using de Vaucouleurs photometry for Abell 1689, but the difference is far less than the uncertainties. Consequently, we take the average of the KR and FJR offsets (excluding BCGs) using both Sérsic and de Vaucouleurs photometry as the overall luminosity evolution. We now seek the uncertainty in this value. The $\langle\mu\rangle_e$ and R_e data used in the KR are strongly correlated to the magnitudes used in the FJR so we cannot treat the uncertainties in $\Delta\beta_{\mathrm{KR}}$ and $\Delta\beta_{\mathrm{FJR}}$ as independent. We combine the MCMC samples for $\Delta\beta_{\mathrm{KR}}$ and $\Delta\beta_{\mathrm{FJR}}$ from the fits to Sérsic and de Vaucouleurs surface photometry, thereby assuming equal evidence for all these models and measure the difference in luminosity between the Coma galaxies (measured in rest-frame r′) and the Abell 1689 galaxies (measured in the observed-frame F625W) to be 0.22 ± 0.11 mag. We do not attempt to quantitatively justify the assumption of equal evidence as the results from the different models are very similar.

4   STELLAR POPULATION MODELS

As discussed in §1, changes in the scaling relations can be understood in terms of evolution of the stellar populations. In order to infer such evolution from the observations, it is necessary to make use of stellar population synthesis models which reproduce the SED given some assumptions regarding that population, such as the age, the IMF, the metallicity (Z) and the star formation history (SFH). The latter describes the distribution of star formation over time and in our case is assumed to be a delta function at some previous time (i.e. a simple stellar populations or SSPs), so has a single characteristic age.

It is beyond the scope of this paper to perform an exhaustive comparison of all the possible models now available. We use two common population synthesis models (Bruzual & Charlot 2003 and Maraston 2005, hereafter BC03 and M05) to study the evolution of the scaling relations. Both provide SSP SEDs[4] spanning a variety of ages, metallicities and IMFs, although we only consider models using a Salpeter IMF.

We use these models together with the filter curves provided by BC03 (SDSS and Gunn bands) and the GEMINI

---

[4] http://www.cida.ve/~bruzual/bc2003 (BC03) and http://www.icg.port.ac.uk/~maraston/ (M05)

Observatory[5] (GMOS-N r′ and g′) and the Vega and Solar spectra provided by the HST calibration database (CAL-SPEC[6]). We make use of the COSMOLOPY[7] python library to calculate look back times and redshifts given our cosmological parameters (see §1). The model magnitudes are calculated so as to be comparable to observations that are K-corrected for bandpass effects (K_b), but not for colour effects (K_c).

Observations of objects at different redshifts equate to observations in different frames of reference (observer, rest), while all the model calculations are performed in the rest frame. This, together with the different magnitude systems (Vega, AB, Gunn) and the different *epochs* at which we observe our galaxies, need particular attention. Consequently, where necessary, we label the specified filter with the magnitude system, the frame of reference and the epoch of the observation in parenthesis. For example, F625W(AB, z=0.0, T) refers to AB magnitudes of local objects in the F625W filter, while F625W(AB, z=0.183, T-2.26 Gyr) refers to observations in F625W for an object at z=0.183 (the look back time for an object at z=0.183 is 2.26 Gyr for our adopted cosmology). The difference F625W(AB,z=0.183,T-2.26 Gyr) - r′ (AB,z=0.0,T) is what we measure when comparing our Abell 1689 data to the Coma data (i.e. $\Delta\beta$). We also find it useful to quote model values for which we do not have observations: F625W(AB, z=0.183, T) refers to observations in the blueshifted F625W filter at the current age of the Universe and so F625W(AB, z=0.183, T)-F625W(AB, z=0.183, T-2.26 Gyr) is just the luminosity evolution between now and 2.26 Gyr ago in the blueshifted F625W filter bandpass (approximately equivalent to the V-band).

These stellar population models can be used in many ways, but we choose two distinct and very different techniques for the CMR analysis and KR/FJR analysis. We present the BC03 and M05 results for modelling the passive evolution of SSPs as a function of age and various metallicities in both cases.

4.1 Analysis of the g′-r′ CMR

As discussed in §1, the intrinsic scatter in the CMR tells us about the SFH of the galaxies. We can perform a similar analysis to BLE92 for Abell 1689, but using state of the art population synthesis models. Fig. 7 shows the rate of change of (g′-r′) as a function of the age of the stellar population for the BC03 and M05 models with solar and super-solar metallicities. Like BLE92 and BKT98, we smoothed the models; the resulting systematic error was no more than 0.1 mag. Our SSP tracks in Fig. 7 are broadly similar to those of BLE92 and BKT98, but the M05 models show a more rapid fall in the rate of change of colour before <4 Gyr, followed by very slow or even negligible further reddening beyond > 4 Gyr.

Following BLE92 and BKT98, we model the formation of galaxies with a uniform distribution of random events distributed over a time interval Δt with mean age (now)

t_f. We parameterise the time interval Δt as a fraction, β, of the time available up to the end of Δt; when galaxies form between times t_{start} and t_{stop}, $\Delta t = t_{stop} - t_{start}$, and $\Delta t = \beta t_{stop}$ with $0 < \beta < 1$ (when $\beta = 1$, galaxy formation is continuous from the start of the Universe to some final time t_{stop} so we have the largest possible scatter in ages and no synchronisation). We can write Δt in terms of t_f,

$$\Delta t = \frac{t_{univ} - t_f}{\beta^{-1} - 1/2} \quad (23)$$

where t_{univ} is the age of the Universe now.

As noted by BLE92, if the slope of the CMR is produced by variation in metallicity with luminosity and all galaxies have have identical IMFs, then the RMS scatter of the CMR, σ_{CMR} is related to the RMS scatter in the formation ages of the RS galaxies, σ_{age} by

$$\frac{\sigma_{CMR}}{\sigma_{age}} \approx \frac{\partial(g' - r')}{\partial t} = f(age) \quad (24)$$

where the RMS scatter $\sigma_{age} \approx \Delta t/3.5$ for the uniform distribution considered here (see BLE92 & BKT98).

The observed scatter in the CMR can therefore tell us about the scatter in the formation times (synchronisation, β). But as galaxies become redder with time and the rate of change of colour decreases, a small scatter in the CMD could also imply a very old population with no synchronisation. Eq. 24 can be written

$$\frac{\partial(g' - r')}{\partial t} \approx 3.5\sigma_{CMR}\left(\frac{\beta^{-1} - 1/2}{t_{univ} - t_f}\right) \quad (25)$$

For a given β, there is an age, t_f, which is compatible with the observed scatter σ_{CMR}. In Fig. 7, we plot the LHS of Eq. 25 (curves of $\partial(g' - r')/\partial t$ derived from stellar population models) and the RHS of Eq. 25 ("beta" curves). Where these curves intersect gives the model age *now* that satisfies Eq. 25. While BLE92 assumed that the variation in the rate of change of colour with metallicity was sufficiently small that they could consider only one metallicity (in effect assuming that the slope of the CMR was zero), we investigate solar and super solar metallicities. Fig. 7 shows all these curves for the BC03 and the M05 models. Significant differences only exist for younger ages (i.e. for $\beta \sim 0.6$). We show the 68% uncertainty limits for individual beta curves as dotted lines (based on the uncertainty in σ_{CMR}).

Fig. 7 shows that σ_{CMR} in Abell 1689 is compatible with a large range of ages, depending on the degree of synchronisation. BLE92 and BKT98 found the same for Coma and that they argued that younger ages and smaller Δt are increasingly unlikely because such high SFRs would be easily visible but are not observed. However, we observe Abell 1689 some 2.26 Gyr earlier than Coma: combining both results as though we had observed the same cluster twice over a 2.26 Gyr interval adds another constraint: if the scatter in the CMR has not significantly changed over the last 2.26 Gyr, then the rate of change of colour also cannot have changed appreciably over 2.26 Gyr. To try and put an upper limit on how much the rate of change of colour could have changed over these 2.26 Gyr, let us consider a lower limit on the Coma CMR scatter of 0.036 mag (the scatter for *just* ellipticals within 600 Mpc in BTK98). The scatter of all RS galaxies 2.26 Gyr earlier (in Abell 1689) is measured to be 0.054 mag; this gives a maximum rate of change of -0.008 mag/Gyr for
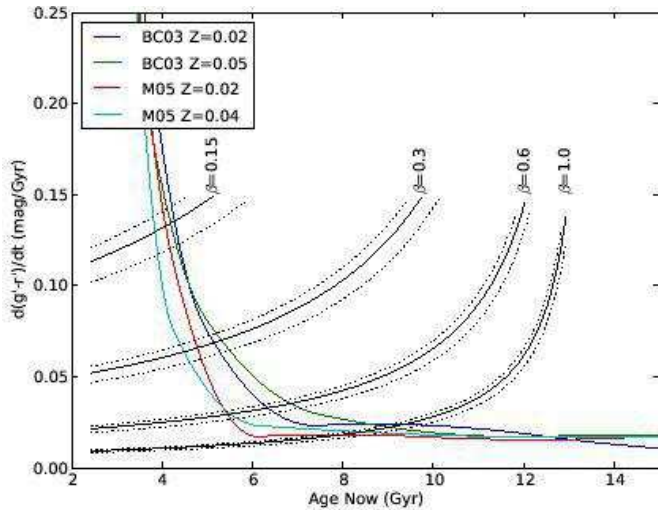
Figure 7. The rate of change of colour vs. the age of the stellar population for the gmos g'-r' colour using BC03 and M05 models for solar and super-solar metallcities. The x-axis represents t_f+2.26 Gyr, which is the age *now*, rather than the age at z=0.183; this is to allow easy comparison with Fig. 8.

the CMR scatter, or -0.028 mag/Gyr for the rate of change of colour. In Fig. 7, models that allow for such a small change over 2.26 Gyr have ages > 6 Gyr and β > 0.6. According to the exact intersections in Fig. 7, the galaxies in the RS of Coma and Abell 1689 formed between $0.55 < z < 1.55$ (have $5.5 <$ age (Gyr) < 9.5), if the Abell 1689 RS evolves into the Coma RS. The scatter could be overestimated in Abell 1689 (we do not select galaxies by morphology or recession velocity), so the upper limit on age, like the lower limit on the scatter, could be questioned; thus we are only confident that the galaxies in the RS of Coma and Abell 1689 are > 5.5 Gyr old (formed at $z > 0.55$). Similarly, only models with $\beta > 0.6$ are consistent with this view.

4.2 Analysis of the KR and FJR

Our principle goal is to determine what (if any) luminosity and colour evolution has taken place between now and z=0.183. We use the BC03 and M05 models to calculate the evolution of F625W(AB, z=0.183, T) - r(AB, z=0.0, T) as a function of the age, T (roughly a V-r colour). This is shown in Fig. 8(a) and shows that after ~ 4 Gyr, F625W(AB, z=0.183, T)-r(AB, z=0.0, T) for the model populations changes slowly from 0.4 to 0.5 mag at 13 Gyr, so any ETG older than 6 Gyr *now*, would not be much bluer at z=0.183. Note that this colour is equivalent to the colour term of the K-correction in Eq. 12, K_c: there is variation with age and metallicity, which is why we do not try to apply it to our measurements. We calculate the luminosity evolution over 2.26 Gyr for F625W(AB, z=0.183, T) and r(AB, z=0.0, T) in Fig. 8(b): here we see the evolution is very similar for all models after 4 Gyr (to within $\sim$0.1 mag) and drops rapidly with age. Finally, we calculate the luminosity evolution we measure when we compare the KRs and FJRs of Coma and Abell 1689 in Fig. 8(c) and Fig. 8(d): the evolution of F625W(AB, z=0.183, T-2.26 Gyr) - r(AB, z=0.0, T) is dominated by the change in luminosity

and not colour after 4 Gyr, according to panels (a) and (b). After 6 Gyr, the solar metallicity models show the slowest rate of change and there is significant difference between the BC03 and M05 solar metallicity predictions; because lookback time is not linearly related to redshift, the evolution with respect to *redshift* is almost asymptotically slow in (d).

In Fig. 8(c) and (d) we also over-plot the measured luminosity evolution ($\Delta\beta$) found between the galaxies of Coma and Abell 1689 (see §3.5). The various stellar population models predict different ages for the Coma and Abell 1689 galaxies from this measurement: considering all models and the 1σ limits, the luminosity evolution between Coma and Abell 1689 is consistent with an age > 6.0 Gyr . Limiting the models to solar metallicities, the BC03 model suggests an age of $8.6\pm^{4.9}_{1.8}$ Gyr , while the M05 model suggests an age of $11.4\pm^{>3.6}_{3.9}$ Gyr (models only run to 15 Gyr): there is a discrepancy between the ages inferred from the BC03 and M05 solar metallicity models, the latter being older by 2.8 Gyr, although both lower limits are comparable. In the absence of any reasonable cause to discriminate between the BC03 and M05 models, we average the ages and uncertainties (i.e. combine the samples, assuming equal evidence for the different models) to conclude that the galaxies in Coma and Abell 1689 are now 10.2 ± 3.3 Gyr old (i.e. formed at $z = 1.8\pm^{\infty}_{0.9}$). Note that because the M05 models are only calculated to 15 Gyr and the 1σ upper limit on $\Delta\beta$ is greater than the model predictions at that age, we can only quote the upper limit from the BC03 model.

It is customary to quote the luminosity evolution in the same band and our stellar population models allow us to calculate this. The BC03 and M05 solar metallicity models both give a luminosity evolution of 0.25 mag in the F625W(AB,z=0.0) band and 0.23 mag in the r' (AB,z=0.0) band for their respective ages.
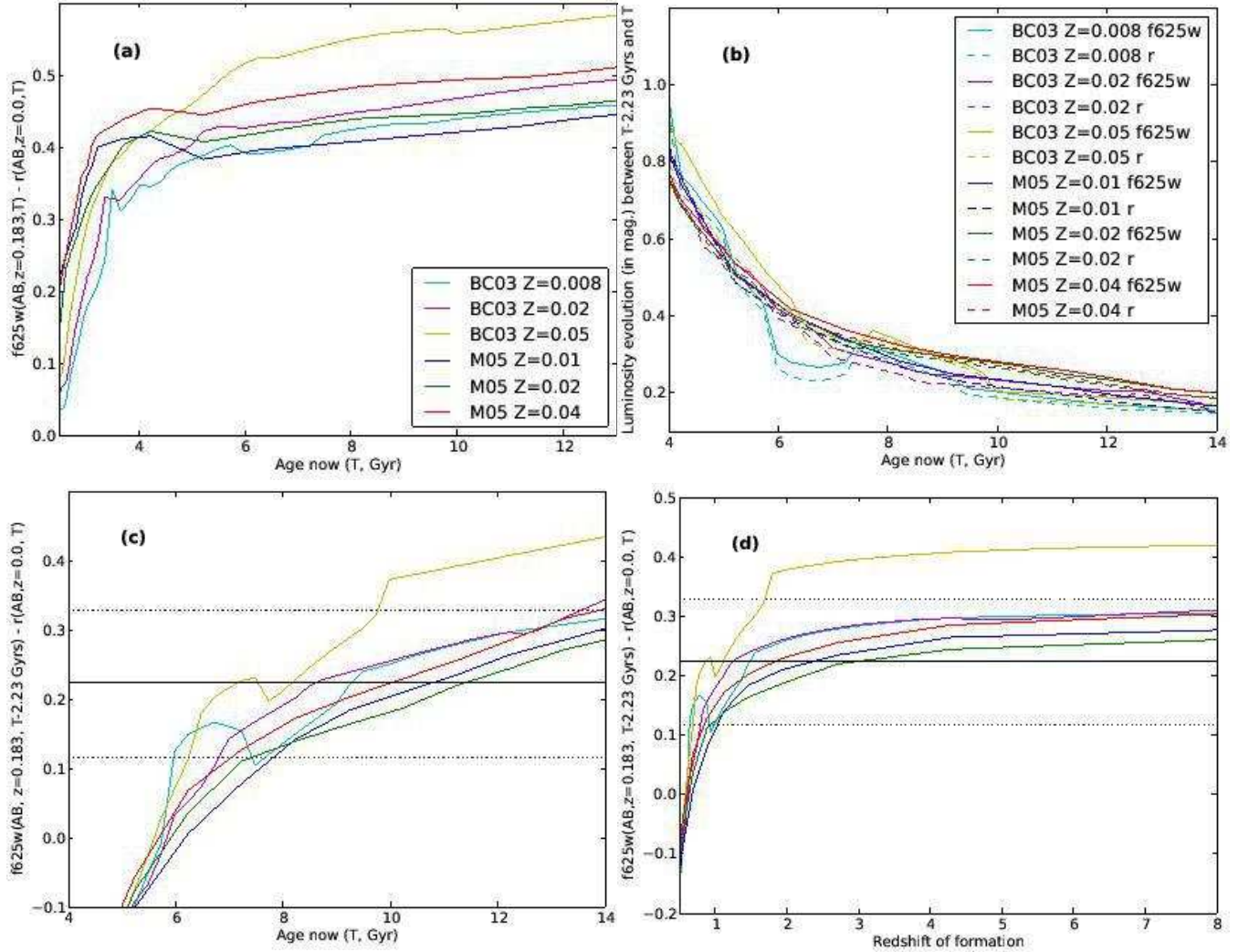
Figure 8. (a): the change in F625W(AB, z=0.183, T)-r(AB, z=0.0, T) colour as a function of age, T; (b): the change in luminosity for the r(AB, z=0.0, T) and F625W(AB, z=0.183, T) filters as a function of T; (c): the difference between F625W(AB, z=0.183, T-2.26 Gyr) and r(AB, z=0.0, T) as a function of T, line colours are as in (a), solid and dashed lines show the evolution and associated uncertainty inferred from the FJR and KR; (d): like (c), but as a function of formation redshift, line colours are as in (a). **All**: magnitudes are in the AB system; two different population synthesis models (BC03 and M05) are shown for sub-solar, solar (Z=0.02) and super-solar metallicities. All models are consistent with galaxy ages > 6.0 Gyr . The BC03 $Z_\odot(=0.02)$ models suggest ages of $8.6\pm^{4.9}_{1.8}$ Gyr while the M05 $Z_\odot$ models suggest ages of $11.4\pm^{>3.6}_{3.9}$ Gyr (models only run to 15 Gyr).

5 DISCUSSION

We now discuss the context of our findings and highlight relevant caveats so that the reliability of our approach can be judged. We discuss the CMD first, followed by the Faber-Jackson and Kormendy relations and summarise the findings at the end.

5.1 The CMR of Abell 1689

The scatter in the CMR of Abell 1689, $\sigma_{\rm CMR}$ =0.054±0.004 mag (for all galaxies with M_V < 17.9 mag within a projected radius of 570 kpc from the cluster centre) is comparable to the bi-weight scatter quoted by Terlevich et al. (2001) of $0.063\pm^{0.008}_{0.01}$ mag. Combining these results, we break the β– age degeneracy and show that the galaxies in both clusters have an age > 5.5 Gyr (and formed at $z > 0.55$) and had

little or no synchronisation in their formation ($\beta > 0.6$). We now ask if this result is in agreement with other clusters at other redshifts. Then we compare Coma and Abell 1689 to judge if we are making a fair comparison. We also discuss the usefulness of placing *lower limits* on the CMR scatter and finally explain why certain caveats in our approach should not strongly bias the outcome.

5.1.1 Abell 1689 in perspective

As discussed in §1.2, Stanford et al. (1995), Ellis et al. (1997), Stanford et al. (1998) and most recently Mei et al. (2009) have studied the CMR scatter in clusters up to $z \sim 1.3$. The last two authors used a clipped bi-weight estimator to measure the CMR scatter; to our knowledge, we are the first to model and extract the CMR scatter using a mixture model which does not rely on arbitrary cuts, clipping

thresholds or parameter tuning. Furthermore, we present a CMR scatter that is marginalised over all reasonable slopes and intercepts, whereas previous work quotes values *given* a measured slope and intercept. That said, the findings of these papers agree with our work: the scatter in the CMR has remained relatively unchanged in the ETG population of massive galaxy clusters since z∼ 1.3. Both Stanford et al. and Mei et al. found the scatter in their clusters to be nearly always less than 0.1 mag with the average being around 0.06 and 0.05 mag, respectively. Both authors were also careful to discuss how selection effects may bias the determination of the CMR scatter at higher redshift (so-called *progenitor-bias*): they selected galaxies morphologically to be Es and S0s, so mergers or spirals were excluded from the sample. We know that more (blue) spirals exist in clusters at higher redshift (Butcher & Oemler 1984) so it is reasonable to consider that the population of galaxies on the CMR at higher redshift is not the same population observed at lower redshift. Furthermore, clusters grow over time and more field ellipticals will join the cluster later on, producing a similar bias. But the bias is less here, because we do not morphologically select our galaxies and at z=0.183 we are only looking 2.26 Gyr into the past, which is less time for change in the ETG progenitors compared to Coma.

5.1.2 Lower limits on the CMR scatter

Until now, no one has tried to interpret a *lower* limit on the scatter of the CMR. We do so now tentatively, because we know that that scatter is likely to be smaller for just ellipticals and also for samples limited to more luminous galaxies. Taken at face value, the lower limit of the scatter measured here suggests that, with $\beta = 1.0$, the highest possible mean formation age for the RS galaxies of Abell 1689 is 9.8 Gyr in the past ($z = 1.7$, a 1σ upper limit). This may be meaningless because we know we have mixed populations (ellipticals, S0s etc.) which increase the scatter, but in future surveys it may be of interest to consider an upper bound on the mean formation redshift if we wish to dedicate effort to witnessing it. If all the stars in the Coma ETGs formed in the first Gyr after the big bang ($t_f = 13.2$ Gyr, $\beta = 1.0$), the CMR scatter would be ∼0.005 mag – seven times smaller than that of Coma. It takes time for dark matter (DM) to cluster sufficiently to allow the baryons to start forming stars, but the difference between a scatter of 0.036 mag and 0.005 mag in the CMR of Coma implies there was a delay of ∼3 Gyr between the big bang and the average SF period for rich clusters (assuming $\beta = 1$). This suggests that the majority of stars formed for $z < 3$ which is in agreement with the cosmic star formation history (Madau et al. 1996, 1998).

5.1.3 Caveats

BKT98 investigated exponentially declining SFHs truncated at different times and also looked at the effects of merging. They found the same conclusions as BKT92, validating the SSP approach used there (and here). We treat the random errors in magnitude and colour as independent, but in reality they will be correlated: noise in the central aperture of the r-band images will affect the colour term as well as the total r-band magnitudes. This will have minimal effect on

our scatter measurement, but could slightly affect the uncertainties. We investigated the assumption that Abell 1689 will evolve into Coma in §2.7.1.

5.2 The Faber-Jackson and Kormendy relations

After correcting for size evolution, magnitude cuts and selection effects, analysis of the FJR and KR in Abell 1689 shows that the Abell 1689 galaxies in F625W are fainter than the Coma galaxies in rest frame r′-band by 0.22 ± 0.11 mag, which suggest and age of 10.2 ± 3.3 Gyr ($z = 1.8 \pm^{\infty}_{0.9}$). We now compare these findings with the literature and discuss the importance of correcting for size evolution.

5.2.1 Evidence for the passive evolution of ETGs

The luminosity evolution in the KR and FJR in Coma and Abell 1689 is consistent with a passively evolving stellar population from single burst 10 Gyr ago. This is in agreement with the long-standing findings that ETGs both locally and at moderate redshift appear to be dominated by old passively evolving stellar populations that formed at $z > 1$. The majority of precision age determinations stem from measurements of absorption line indices: although the broad-band colours of the Coma ETGs have been known to be compatible with old populations for a long time (see §1.1), the well documented age–metallicity degeneracy limits this approach for local clusters, but the degeneracy can be reduced by modelling the absorption line indices of the metals. Little work has been done specifically on the galaxy populations of Abell 1689: Mieske et al. (2004) studies the ultra-compact dwarf fraction and luminosity function of the cluster galaxies while Bañados et al. (2010) study the faint end of the luminosity function. Carretero et al. (2007) studied line indices of ETGs in 4 massive clusters at $z \sim 0.2$ and found ages of around 10–15Gyr, but their sample did not include Abell 1689. Considerably more work has been done on the galaxy populations of Coma, in particular with regard to determining the stellar population ages (Clemens et al. 2009; Jørgensen et al. 1999b; Mehlert et al. 2003; Sánchez-Blázquez et al. 2006, 2009; Rakos et al. 2007; Trager et al. 2008; Smith et al. 2009; Harrison et al. 2010, 2011; Price et al. 2011). There is still some uncertainty regarding the ages (and presence of multiple populations), but the current evidence suggests ages between 5 and 10 Gyr for the Coma ETGs. Our age estimate from the broad band photometry of Abell 1689 and Coma is therefore towards the top of this range, though the BC03 result alone ($8.6\pm^{4.9}_{1.8}$ Gyr) is nearer the midpoint and the M05 result at the upper end ($11.4\pm^{>3.6}_{3.9}$ Gyr (models only run to 15 Gyr)); intriguingly, the age range implied by just the scatters of the CMRs in Abell 1689 and Coma ($5.5 <$ age (Gyr) < 9.5) brackets the literature ages very well, even though earlier we expressed doubt regarding this upper limit (see §4.1).

5.3 The effects of size evolution

The measured luminosity evolution between Abell 1689 and Coma agrees with that of other clusters (Barrientos et al. 1996; Pahre et al. 1996; Ziegler et al. 2001; La Barbera et al. 2003; Fritz et al. 2005), although

none of these studies corrected for size evolution. Most did not simultaneously study both the FR and FJR except for Fritz et al. who found that the galaxies appeared brighter in the KR than in the FJR (but the 0.07 mag difference is considerably less than the 0.3 mag found here). Saglia et al. (2010) allow for size evolution in their study of the FP out to $z \sim 1$. However, we are not probing a high redshift cluster, but a comparatively local cluster at z=0.183. The fact that we need size evolution to bring the KR and FJR into agreement suggests that whatever causes it is a gradual process and its effects are not limited to the high-z universe; indeed, the mechanism is probably still in action now and does not appear to have deviated from the high-z $(1+z)^{\zeta,\eta}$ laws.

While there has been a reasonable passage of time between z=0.183 and now (2.26 Gyr), observing the size evolution taking place *in the cluster environment* and *in the local Universe* place important restrictions on models that wish to explain size evolution, which we now discuss.

Merging: Wet or dry major merger scenarios (e.g. Khochfar & Silk 2006; Hernquist et al. 1993; Hopkins et al. 2009) are unlikely to occur in the cluster environment because cluster galaxies have a very high relative velocity (larger than the typical escape velocity of two massive galaxies) making it prohibitively difficult to merge galaxies. An exception are central BCGs which would likely merge when multiple clusters merge as they lie at rest at the bottom of the potential. Minor or late accretion of smaller galaxies (e.g. Naab & Trujillo 2006; Maller et al. 2006; Naab et al. 2009; Hopkins et al. 2009, 2010) could be more feasible because of the larger number of low-mass satellites, but in general the relative velocities would still be higher than the escape velocity unless the impact was at glancing angle.

Accretion: Accretion of the intra-cluster stars (previously stripped from other galaxies) may be energetically plausible, if not in mass transfer rates. However, while the simulations of Bois et al. (2011) and Khochfar et al. (2011) suggest that ATLAS3D *slow rotators* grow from minor accretions, Stott et al. (2011) finds no evidence of size evolution in BCGs up to $z < 1$.

Adiabatic expansion: The action of AGN expelling gas as proposed by Fan et al. 2008 is perhaps unfeasible here because we know that massive reservoirs of gas are stripped when galaxies fall into a cluster (observed for gas rich spirals falling into the cluster potential today, Chung et al. 2009). However, the mass lost from evolving stars could be gradually stripped by the ICM. Adiabatic expansion could also occur when central mass (dark or luminous) is stripped or *harassed* to larger radii by high speed encounters, which are inevitable in clusters.

Secular/Cosmological expansion: There are few secular arguments (the action of bars and/or resonances) for size evolution in the literature at present and perhaps these should be investigated further given our findings: if S0s are believed to be faded spirals (the vast majority of Es show fast rotating disc-like disk kinematics, Emsellem et al. 2007, 2011), then whatever action reduces disks to spheroids could also be responsible for the size evolution we observe. Recall also that size evolution in disks was predicted as a consequence of them being truncated to the critical density (Mo et al. 1998), which is entirely a secular/cosmological effect.

5.3.1   Caveats

Some caveats to consider for our KR and FJR analysis include not correcting for colour gradients, invoking size evolution, *not* selecting galaxies morphologically or to be on the RS, and using non-independent PDFs as though they were independent. We have already investigated the assumption that Abell 1689 will evolve into Coma in §2.7.1.

An important difference between the FJR and KR is that the latter is potentially sensitive to internal colour gradients; this may be a source of error in our work given that our F625W observations of Abell 1689 are approximately rest-frame V-band compared to the Coma r-band observations. The colour gradients in ETGs cause them to be redder towards the centre; this makes R_e larger at bluer wavelengths. Using the Coma data from Jørgensen et al. (1995a), we find that R_e in Gunn g is a mean of $\sim 5 \pm 15\%$ (or a median of 2%) larger than R_e in Gunn r. However, if one considers the combined effects in the KR, we find that they cancel to first order. Using the same s.ps that gave rise to Eq. 20, increasing R_e by 5% leads to an *apparent* luminosity evolution of $\log(1.05) = 0.02$ mag in the KR. If we calculate the difference between the central colour $(\langle\mu\rangle_e(\mathrm{g}) - \langle\mu\rangle_e(\mathrm{r}))$ and the global colour (g-r) from the Jørgensen et al. (1995a) data, we find a mean $[\langle\mu\rangle_e(\mathrm{g}) - \langle\mu\rangle_e(\mathrm{r})] - [\mathrm{g} - \mathrm{r}] =$ of 0.05 ± 0.35 mag (median of 0.07 mag). Allowing for the large scatter, this agrees with the above and is a negligible correction. Therefore we conclude that it is not necessary to correct for colour gradients.

We have invoked the existence of size evolution to make sense of the different luminosity evolution seen in the KR and FJR. However, we have chosen a prescription for how the size and internal kinematics of the galaxies change with time based on the evidence to hand (§2.8.3). Although this is the simplest approach, one could try to measure this prescription from the data by making the simple assumption that variation in the mass-to-light is determined only by passive evolution of the stellar population, is independent of galaxy luminosity (or stellar/dynamical mass) and is the same for the KR and the FJR.

Readers may have noticed that we do not select Abell 1689 galaxies in the KR and FJR to be morphological E/S0s or to be on the RS (even though we have that information from the CMR analysis). This is deliberate: we do not want to bias ourselves away from including (blue, spiral) progenitors of ETGs in Coma. However, blue spirals tend to exclude themselves from our sample because they have velocity dispersions below our spectral resolution (most likely because the luminosity is dominated by light from central dynamically cold star forming regions). Of the 38 galaxies that have sufficient quality spectra and HST imaging to enter the fitting procedures, only one is found *not* to be on the RS (#435). Thus although we tried not to select just RS galaxies, we end up being significantly biased towards them.

When calculating the difference between the evolution seen in the KRs and the FJRs, we treated the PDFs as though they were independent normal distributions. Neither of these assumptions is true (the Coma and Abell 1689 data used in both are obviously correlated), but it is the best approach we are reasonably able to take.

6   CONCLUSIONS

We have presented the Kormendy, Faber–Jackson and colour-magnitude relations for ETGs in Abell 1689 using HST/ACS imaging, GEMINI/GMOS imaging and GEMINI/GMOS spectroscopy and conclude:

(i) The intrinsic scatter in the colour–magnitude relation of Abell 1689 places degenerate constraints on β (the ratio of assembly timescale and time available) and the age of the population: specifically, it is consistent with the galaxies in the colour–magnitude relation having either formed randomly at high redshift ($z \gtrsim 2$), or at lower redshift with increasing synchronisation (smaller assembly timescales). However, assuming the intrinsic scatter of Coma and Abell 1689 is that of the same cluster observed twice over an interval of 2.26 Gyr breaks this degeneracy and limits β to be > 0.6 (little or no synchronisation) and the age of the red sequence to be > 5.5 Gyr (formed at $z > 0.55$).

(ii) After accounting for size evolution effects, the F625W Kormendy and Faber–Jackson relations both show a similar change in luminosity compared to the rest frame r′-band relations of Coma: 0.22 ± 0.11 mag. This is consistent with passive evolution of the stellar populations from a single burst of star formation long ago: the galaxies in Coma and Abell 1689 have an SSP age of 10.2 ± 3.3 Gyr (i.e. formed at $z = 1.8\pm^{\infty}_{0.9}$), which agrees with the CMR analysis above. However, not accounting for size evolution causes the Kormendy and Faber–Jackson relations to be inconsistent and they then disagree about the amount of luminosity evolution at the 2σ level.

(iii) We therefore find weak evidence that size evolution appears to have taken place in the cluster environment in the last 2.26 Gyr; if true, this places interesting constraints on the models, favouring harassment or secular mechanisms over major or minor merger scenarios.

APPENDIX A: THE CURVE OF GROWTH (COG) TECHNIQUE AND ASSOCIATED ERRORS

The COG method we use is in essence very simple: locate the centre of the galaxy via some means (in our case, via ellipse fitting); integrate out in radius to create a curve-of-growth function; fit an analytical curve-of-growth (Eq. 10), varying the model parameters (apparent magnitude, m; effective radius, R_e and Sérsic index n) to minimise the square of the residuals (χ^2):

$$\chi^2 = \sum_{i=1}^{N} [D_i - M_i]^2 \qquad (A1)$$

where the sum is performed over samples i for the observed COG D_i and model COG M_i. We sample the COG at the plate scale of the input image.

We now discuss how we deal with: PSF effects, contamination and masking of other nearby galaxies, and estimating our uncertainties.

A1   PSF effects

The instrumental PSF of the image creates a systematic difference between the observed and true COG. Saglia et al.
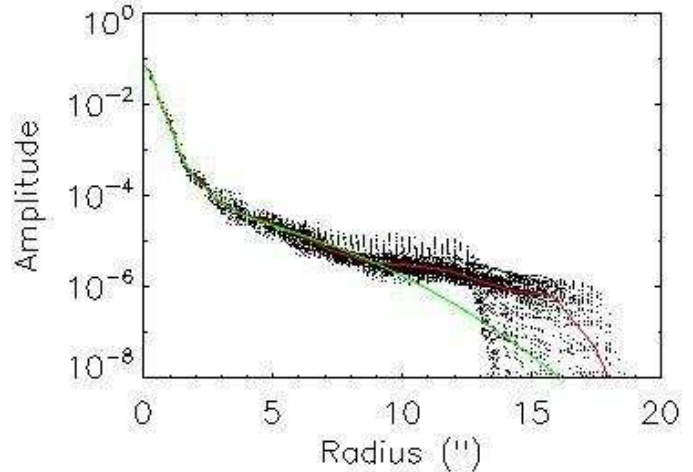

Figure A1. An azimuthal average of multiple HST/ACS PSFs (black points); radially binned points (red) and MGE approximation (green). This MGE approximation is used with Eq. A2 to account for PSF effects when fitting COGs.

(1993), Trujillo et al. (2001a) and Trujillo et al. (2001b) describe methods to correct for this. However, the HST/ACS PSF is not well approximated by a single Gaussian or Moffat function, for which these methods were developed. We approximate the ACS PSF with a multi-Gaussian expansion (MGE, Bendinelli 1991). We azimuthally average (4-fold reflect) multiple PSFs from across the FOV (see §2.2), bin radially, and then use a 1D MGE fitting routine to calculate a radial approximation (made available by M. Cappellari Cappellari 2002). Fig. A1 shows an example.

We make use of the well known result that the convolution of the Sérsic function $I(R, R_e, n)$ with a Gaussian $G(r, \sigma)$ is $I'(R, R_e, n, \sigma) =$

$$\frac{1}{\sigma^2} \int_{x=0}^{x=\infty} I(x, R_e, n) \exp\left[\frac{1}{2}\left(\frac{x^2 + R^2}{\sigma^2}\right)\right] B\left(\frac{xR}{\sigma}\right) \quad (A2)$$

where B is a modified Bessel function of the first kind, zeroth order (Moffat 1969; Bendinelli et al. 1982). Summing this according to the amplitudes of the MGE then provides a good approximation to the full PSF convolution. We do not account for ellipticity in the fitting process. A Levenberg-Marquardt algorithm (MPFIT[8]) minimised χ^2 to fit R_e, I_e and n (we fix $n = 4$ for a de Vaucouleurs profile).

We find good agreement between this 1D approach and Sérsic profiles convolved with the full 2D HST/ACS PSFs: systematic errors in recovered parameters (R_e, I_e, m, $R_e I_e^{0.8}$) are always $<1\%$ over a wide range of parameter space.

A2   Contamination and Masking

The galaxies in Abell 1689 are densely packed and many overlap in projection. To remove this contamination, we initially bin azimuthally averaged profiles of the chosen galaxy and sigma-clip from the mode of each bin. If necessary, we further manually mask the images, ensuring identical masks
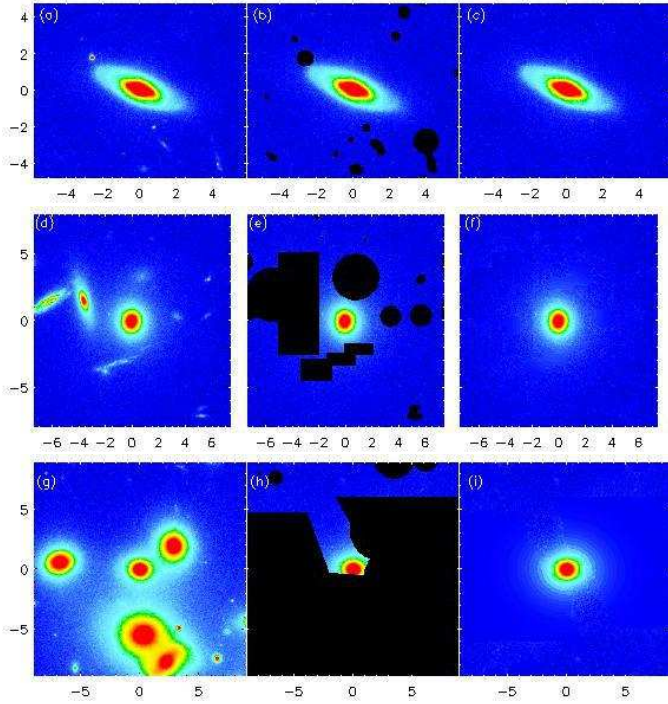
[8] http://www.physics.wisc.edu/~craigm/

Figure A2. Examples of the masking procedure before fitting a curve of growth model. **(a)** HST/ACS F625W image of galaxy #286 which is relatively uncontaminated; **(b)** shows the mask applied to this image (black pixels) and **(c)** shows the result of the image reconstruction from replacing masked pixels with a 2-fold reflection. **(d)** HST/ACS F625W image of galaxy #435 which has considerable contamination; **(e)** shows the mask for this image and **(f)** shows the reconstructed image, produced by replacing pixels with a 2-fold reflection or azimuthally averaged values. **(g)** galaxy #635 is so badly contaminated that a reliable measure of the COG is almost impossible; **(h)** shows the mask (leaving enough information to provide an azimuthal average) and **(i)** shows our best reconstruction. Although the reconstruction in (i) and the associated COG appear convincing, such results always score a 3rd class rating because of the large uncertainties. Scales on the x- and y-axis are in arcseconds, centred on the galaxy. The greyscale is logarithmic and fixed throughout, to highlight faint structure.

for both the de Vaucouleurs and the Sérsic COG fits to prevent systematic differences. To replace masked pixels, a simple 2-fold reflection about the galaxy centre was usually sufficient. When masking was more severe, after a 2-fold reflection, we azimuthally binned the image, averaged the modes of bins at each radius, and replaced masked pixels with this average. This reconstructed strongly contaminated images and gave good COG fits. However, as a method of quality control when the galaxy image was minimally contaminated and the model COG fitted the measured COG to within 2%, we rated the fit 1st class; when the contamination was again relatively minor but the model COG didn't fit the measured COG to within 2%, the fit was rated 2nd class; finally, when contamination was severe, such that we had little confidence in the measured COG and thus the model fit, we rated it 3rd class (shown in Table 4). Examples of masking and image reconstruction are shown in Fig. A2.

A3   Estimating errors (random and systematic)

We use Monte-Carlo simulations to estimate uncertainties in the COG parameters. Generating Sérsic profiles of various R_e, I_e and Sérsic index n convolved with a typical 2D HST/ACS PSF (see §2.2), we add random sky offsets and read and shot noise to simulate real observations. We use 100 realisations for each parameter combination (R_e, m and n) over the parameter space of the obervations. We also vary the radius at which we stop the COG fitting according to the statistics of the real data. This approach allows us to estimate random and systematic uncertainties (the latter always being $< 1\%$).

The simulations show that $\log R_e$ and $\log I_e$ are very strongly correlated. Decomposing the covariance matrix into principle components, the first component always accounts for $>98\%$ of the variation: $R_e I_e^{0.6\pm0.1}$ is best constrained while $R_e^{-0.6\pm0.1} I_e$ is most poorly constrained. Knowing the covariance matrix as a function of input R_e and m allows us to use it when fitting the scaling relations; treating R_e and I_e as independent significantly overestimates the error in the direction perpendicular to the KR which is important when minimising perpendicular residuals (see §C).

APPENDIX B: MATCHING SPECTRAL RESOLUTIONS

The GMOS arc and sky lines appeared top-hat like because the slit width, not the grating, dictated the spectral resolution. Matching spectral resolutions in this case is difficult: firstly, the size or shape of the objects being observed in the GMOS slits can define the resolution and spectral PSF if they are smaller than the slit width; secondly, the kernel required to match the spectral PSF of the stellar library with the GMOS spectra will not be Gaussian. Fortunately, the seeing FWHM (estimated by Gaussian fits to the profiles of guiding/alignment stars) is greater than the $0.''75$ slit width (varying between $0.''74$ and $1.''49$ with an average of $1.''06$). Thus the illumination of the slits was roughly uniform and similar to that of the arc or sky lines, which enables us to use arc or sky lines as a reference for the spectral PSF of the galaxy spectra. An additional complication in matching spectral resolutions is that the width of the GMOS arc lines decreases over the wavelength range used to extract kinematics; if one matches local stellar templates to the observer-frame arc spectra then when later redshifting the templates to the galaxy rest-frame, the non-uniform spectral resolution would introduce a systematic difference between the stellar and galaxy resolutions.

We developed a technique to account for all these effects by finding a *transfer function* which, when convolved with the spectral profile of the stellar library, reproduces the spectral profile of the galaxy spectra (which is equivalent to reproducing line profiles of a *blueshifted* arc spectrum). We found the GMOS arc lines were well described by a truncated Gauss–Hermite (GH) expansion (Gerhard 1993; van der Marel & Franx 1993):

$$T(\lambda) = \frac{\gamma}{\sqrt{2\pi}\sigma} \exp\left[-\left(\frac{(\lambda - \lambda_0)}{2\sigma}\right)^2\right] \sum_{i=0}^{N} h_i H_i(\omega), \quad \text{(B1)}$$

which is a Gaussian centred on λ_0 with scale factor γ, disper-

sion σ weighted by a sum of Hermite polynomials H_i. Taking $h_0 = 1$, we quantify deviations from a Gaussian using the truncated series $\{h_2, h_4, h_6\}$ (odd Gauss-Hermite moments are not required to describe a symmetric shape). Furthermore, given that positive values of h_i (where i is even) provide more top-hat like profiles, whereas negative values give profiles with large wings and sharp peaks, only positive h_i values are required.

We then saught a Gauss-Hermite expansion which, when convolved with another Gaussian of FWHM equal to that of the stellar library resolution (1Å), matched the *blueshifted* arc lines. We accomplished this by minimising the χ^2 difference given by the expression

$$\chi^2 = \sum_{i=1}^{N} \left[A_i' - \left(S_i(\sigma') \otimes T_i(\sigma, h_j) \right) \right]^2 \qquad \text{(B2)}$$

where A' is the (blueshifted) arc line being fit, S is the spectral profile of the stellar library (width σ'), T is the Gauss-Hermite transfer function (Eq. B1) and the sum is performed over pixels. Fig. B2 illustrates the parametric results of this process at various wavelengths (and what would happen if we were not to account for the redshift effect). It is evident that a single transfer function with parameters $\{\sigma, h_2, h_4, h_6\} = \{0.428\text{Å}, 0.676, 0.0, 0.435\}$ is sufficient to degrade the spectral resolution of the stellar library to the blueshifted GMOS arc spectrum. We did occasionally experience a problem of multiple minima when fitting the convolved Gauss-Hermite transfer functions but careful choice of starting parameters solved the problem. Note that because the width (Å) and properties of the transfer function are uniform in λ space, we convolved the stellar library with T *before* resampling it to $\log - \lambda$ space. Fig. B2 compares the profile of the matched stellar library to a typical profile for a (blueshifted) GMOS arc line: they are barely distinguishable from each other, confirming we are able to match the spectral profile of the stellar library to that of the galaxy spectra.
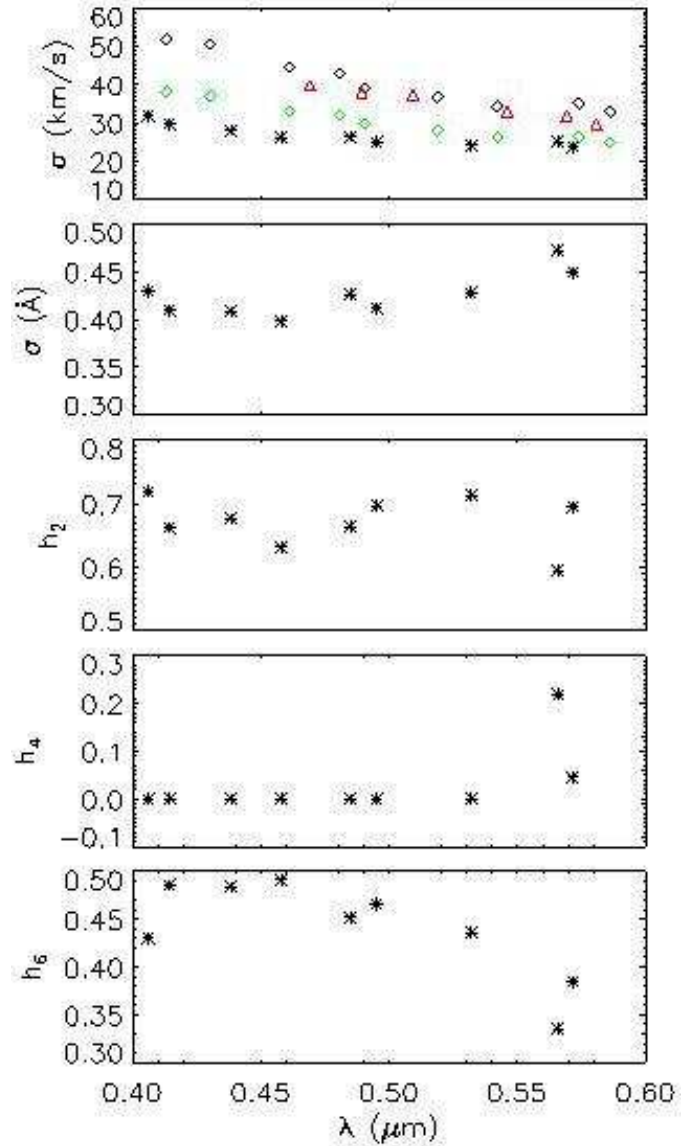
Figure B1. The best-fit transfer function, matching the spectral response of the stellar library to GMOS arc emission lines at various wavelengths. Parameters for the best-fit transfer functions (Eq. B1) to blueshifted arc spectra are approximately uniform for all wavelengths (asterisks) and are well approximated by a single function with parameters $\{\sigma, h_2, h_4, h_6\} = \{0.428\text{Å}, 0.676, 0.0, 0.435\}$. The widths of the GMOS arc lines (σ, black diamonds) are not constant (in λ or $\log - \lambda$ space), which can introduce a systematic error when stellar templates are redshifted to the recession velocity of the cluster. The correct transfer function parameters, accounting for this effect are shown as green diamonds (previously the black asterisks fitted to blueshifted arc spectra, but now redshifted back). The widths of the transfer functions if we had not corrected for the redshift effect are shown as red diamonds: these appear roughly equal to the raw arc widths (black diamonds) but this is bad because the transfer function still needs to be convolved with the response of the stellar library; after this, the stellar templates would have a larger spectral resolution than the galaxy spectra, introducing a systematic error into the kinematics (dispersions would be too low).
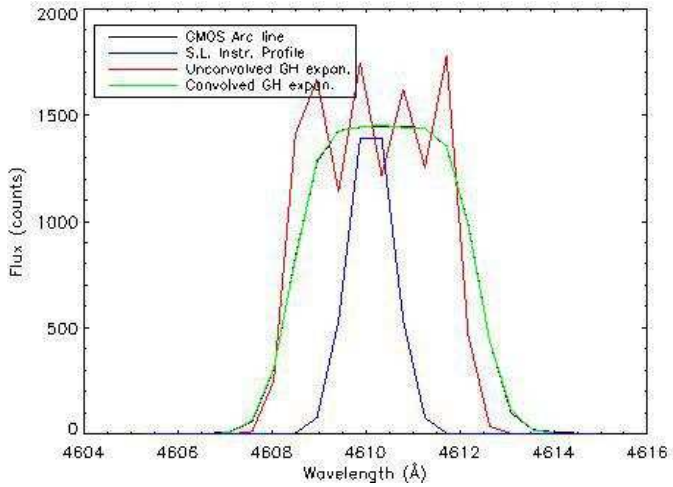
Figure B2. A fiducial GMOS arc line (black) with the raw stellar library instrument profile (blue), best-fit Gauss-Hermite transfer function (red) and matched stellar library profile (green) over plotted. Note that the matched stellar library profile is virtually identical to the GMOS arc line profile.

APPENDIX C: FITTING SCALING RELATIONS USING AN MCMC APPROACH

In §2.9, we briefly discussed the different models we use to fit the scaling relations in Coma and Abell 1689. Here we discuss those models in more detail. We have taken on board the recent remarks made by Hogg et al. (2010) and we turn to Markov Chain Monte Carlo (MCMC) methods to 'fit' the data. We use three different models; each one is discussed below.

C1   The (Simple) Linear model

This model is described by Hogg et al. (2010) in their Eq. 35. We assume that our data $\{x_i, y_i\}$ with (normally distributed) uncertainties $\{\sigma_{xi}, \sigma_{yi}\}$ and covariance $\sigma_{xyi}^2 = \rho_{xyi}\sigma_{xi}\sigma_{yi}$ come from a linear relation $y = \alpha x + \beta$, with *intrinsic* scatter σ_I. Given a data point x_i with uncertainty σ_{xi} we can define the expected frequency[9] of observing the corresponding data point in the range $[y_i, y_i + y]$ with uncertainty σ_{yi} given some particular model parameters $\{\alpha, \beta, \sigma_i\}$ as

$$p(y_i|x_i, \sigma_{xi}, \sigma_{yi}, \alpha, \beta, \sigma_I) = \frac{1}{\sqrt{2\pi(\sigma_{di}^2 + \sigma_I^2)}} \exp\left[-\frac{\Delta_i^2}{2(\sigma_{di}^2 + \sigma_I^2)}\right] \quad (C1)$$

where

$$\Delta_i = \mathbf{v}^T.\mathbf{Z}_i - \beta' \quad (C2)$$

measures the perpendicular distance between the linear model and a data point because

$$\mathbf{Z}_i^T = [x_i, y_i] \quad (C3)$$
$$\mathbf{v}^T = [\cos\theta, \sin\theta] \quad (C4)$$
$$\beta' = \beta\cos\theta \quad (C5)$$
$$\alpha = \frac{\sin\theta}{\cos\theta} \quad (C6)$$

---

[9] see Hogg et al. (2010), note #13

while the combined projected variance perpendicular to the linear model is

$$\sigma_{di}^2 = \mathbf{v}^T.\Sigma_i.\mathbf{v} \quad (C7)$$

and $\mathbf{\Sigma}_i$ is just the covariance matrix

$$\mathbf{\Sigma}_i = \begin{bmatrix} \sigma_{x,i}^2 & \sigma_{xy,i}^2 \\ \sigma_{yx,i}^2 & \sigma_{y,i}^2 \end{bmatrix} \quad (C8)$$

Equally, we could have introduced the rotated coordinate system of the linear model, $Z' = [x', y']$ which describe coordinates parallel and perpendicular to the regression line. They are related to the non-rotated coordinates by $[x', y'] = \mathbf{R}.[\mathbf{x}, \mathbf{y}] - \beta'$ where $\mathbf{R}$ is the usual rotation matrix which depends only on θ. There is an obvious equality between Δ_i and y_i'. There is no need to persist with this rotated coordinate system here, but it will be useful in the next section.

The *likelihood* of observing all our data points given a particular choice of linear model is then the product of the frequency distributions,

$$\mathcal{L}_{LM} = \prod_{i=1}^{N} p(y_i|x_i, \sigma_{x,i}, \sigma_{y,i}, \alpha, \beta, \sigma_I). \quad (C9)$$

Standard fitting procedures based on minimising χ^2 or 'maximising the likelihood' then vary the model parameters to maximise this expression and find the mode of the likelihood distribution. However, the Bayesian view on this is to say that the *posterior* probability distribution of the model is

$$p(\alpha, \beta, \sigma_I|\{y_i\}_{i=1}^N, Q) = \frac{\mathcal{L}.p(\alpha, \beta|Q)}{p(\{y_i\}_{i=1}^N|Q)} \quad (C10)$$

where Q is shorthand for all the other (not always prior) knowledge of the problem, such as the x_i, $\{\sigma_{x,i}, \sigma_{y,i}\}$ etc. Readers familiar with Bayes Theorem will recognise all the terms above, but for the unacquainted, $p(\alpha, \beta|Q)$ contains additional information about the problem (and is referred to as the prior) and $p(\{y_i\}_{i=1}^N|Q)$ is the normalising constant we evaluate by insisting that our final posterior distribution is normalised to one. Note that maximising the likelihood is equivalent to maximising the posterior given uniform priors on all parameters.

MCMC samplers can probe the above likelihood with different model parameters and provide a set of sample points that are distributed according to the posterior probability distribution (PDF) because they were drawn from it. This is our preferred method here, for two reasons. Firstly, it relaxes the standard assumption that the parameters are normally distributed; while normality may be a good approximation for m and b, it is certainly not so for σ_I because $\sigma_I \geq 0$, providing a hard (asymmetric) edge to the allowed distribution which we can set as a prior. Secondly, using MCMC here in a relatively simple model prepares us for more complicated models.

In terms of implementation, we use the PYMC library (Patil et al. 2010) to sample parameters θ, β', σ_I using the standard Metropolis-Hastings MCMC algorithm. We choose relatively unrestrictive priors that are flat but always over a finite range: we let θ range between $\theta_0 \pm \pi/2$ (where θ_0 is a good initial guess; this avoids searching for solutions near the boundaries); the intercept (β') is limited to a finite range because we can't sample to $\pm\infty$; the intrinsic scatter (σ_I) is

not allowed to be negative and also has some sensible upper limit.

Whenever we quote a *best-fit* or *most probable* value for one of the parameters, we quote the median of the resulting samples (which by default is marginalised over all other parameters). The MCMC usually requires reasonably good initial guesses to converge rapidly and such a guess can be provided by the 'maximum likelihood' estimates or by eye.

As highlighted by Hogg et al. (2010), outliers can cause havoc in this simple linear model and §C3 discusses our implementation of the solution proposed by those authors.

C2 The (Complex) Double Linear Model

It is often the case when studying scaling relations that one wishes to compare the intercept or offset of one relation to another. A common solution is to calculate the offset at a particular value along the x-axis, but such a result is dependent on the different slopes assumed for the two relations (as well as their intercepts). Alternatively, if there is good reason to believe the slope of the relations hasn't changed, one might fit the slope of the local relation (which usually has more data) and then impose this fixed slope on the high redshift data (e.g. Barr et al. 2006); then at least there is no error created by imposing two *different* slopes, although there is *still* a strong dependence on the slope itself, the intercepts and any internal scatter being derived.

To circumvent these problems, we propose a model consisting data drawn from two populations, $Z_{1,i}^T = [x_{1,i}, y_{1,i}]$ and $Z_{2,i}^T = [x_{2,i}, y_{2,i}]$, each of which is described by a linear relation (as in §C1) but we constrain the linear relations to have the same slope α and internal scatter σ_I; we then let the first population have intercept β_1 while the second population with intercept β_2 is offset to this by $\Delta\beta$, such that $\beta_2 = \beta_1 + \Delta\beta$. In this way, the two linear models share the same properties, except for the intercept and we have parameterised the variable we are most interested in as $\Delta\beta$. The likelihood for this model thus far would be

$$\mathcal{L}_{\mathrm{DLM}} = \sum_i p_{1,i} \times \sum_j p_{2,j} \qquad (C11)$$

where

$$p_{1,i} = \frac{1}{\sqrt{2\pi\sigma_{1,i}^2}} \exp\left[-\frac{\Delta_{1,i}^2}{2\sigma_{1,i}^2}\right] \qquad (C12)$$

$$p_{2,j} = \frac{1}{\sqrt{2\pi\sigma_{2,j}^2}} \exp\left[-\frac{\Delta_{2,j}^2}{2\sigma_{2,j}^2}\right] \qquad (C13)$$

give the frequency distributions of the individual data points for the two populations: $\Delta_{1,i} = \mathbf{v}^T.\mathbf{Z_{1,i}} - \beta_1'$ defines the residuals for the first population and $\Delta_{2,j}$ similarly defines the residuals for the second population; the expressions

$$\sigma_{1,\,i}^2 = \sigma_{1,\mathrm{di}}^2 + \sigma_I^2 \qquad (C14)$$

$$\sigma_{2,\,j}^2 = \sigma_{2,\mathrm{dj}}^2 + \sigma_I^2 \qquad (C15)$$

give the total variances perpendicular to the relation. Hopefully the definitions of σ_I, $\sigma_{1,\mathrm{di}}$ and $\sigma_{2,\mathrm{dj}}$ are obvious to the reader from §C1.

One would also like to account for magnitude cuts and selection effects which are known to cause bias in the derived parameters (Willick 1994; Teerikorpi 1997; Saglia et al.

2001; La Barbera et al. 2003; Butkevich et al. 2005). In the KR and FJR, magnitude cuts have the effect of masking a region of parameter space from being studied. In both cases, the division between the unsampled and sampled regions can be defined by a linear relation of the form $y = \alpha_{\mathrm{cut}} x + \beta_{\mathrm{cut}}$. For the KR,

$$\alpha_{\mathrm{cut}} = 5 \qquad (C16)$$

$$\beta_{\mathrm{cut}} = m_{\mathrm{cut}} + 2.5\log(2\pi) \qquad (C17)$$
$$-7.5\log(1+z) - 5\log\left(\frac{\mathrm{kpc}}{\mathrm{arcsec}}\right)$$

while for the FJR,

$$\alpha_{\mathrm{cut}} = 0 \qquad (C18)$$

$$\beta_{\mathrm{cut}} = m + 2.5\log(1+z) - 5\log D_L + 5 \qquad (C19)$$

The ratio of the spectroscopic samples to the parent samples as a function of m for both Abell 1689 and Coma can be fit by a *selection function* of the form (Wegner et al. 1996)

$$S_i = \frac{1}{2}\left\{1 - \mathrm{erf}\left(\frac{m_i - m_{\mathrm{cut}}}{\sqrt{2}\delta_m}\right)\right\} \qquad (C20)$$

where erf is the error function, m_{cut} is the position of the cut (also the 50% completeness limit) and δ_m is the width/uncertainty of the cut (recall that Eq. C20 describes a Heaviside step function at m_{cut} convolved with a Gaussian with $\sigma = \delta_m$). We fit the selection function (Eq. C20) to the spectroscopic samples of Coma and Abell 1689 following the approach described in Wegner et al. (1996). For Abell 1689, using SEXTRACTOR magnitudes, we find that the spectroscopic sample is consistent with selecting 60% per magnitude bin of the parent sample down to $m_{\mathrm{cut}} = 19.5$ mag with uncertainty $\delta_m = 0.62$ mag; for Coma, we find the spectroscopic data of Jørgensen et al. (1996) consistent with sampling 100% of the population down to $m_{\mathrm{cut}} = 14.8$ (AB) mag with uncertainty $\delta_m = 0.5$ mag.

We model the magnitude cuts of the two samples in a similar way to Saglia et al. (2001) and La Barbera et al. (2003) by scaling the frequency distributions (i.e. the p_i) by a factor $1/f_i$ to account for the parameter space masked by the cut. This requires us to make an assumption about the distribution of the data *along* the regression line which we assume is uniform, starting at $x'_{\mathrm{min}} = \min(x'_i)$ and ending at $x'_{\mathrm{max}} = \max(x'_i)$ thus having width $L = \max(x'_i) - \min(x'_i)$ (which is not a free parameter, but is set by the data and values of α and β). Therefore the probability space masked by the magnitude limit as a fraction of the total probability space is

$$f_i = \frac{1}{L\sigma_i\sqrt{2\pi}} \int_{x'=x'_{\mathrm{min}}}^{x'_{\mathrm{max}}} x' \int_{y'=y_{\mathrm{cut}}}^{y'=\infty} y' \exp\left(-\frac{y'^2}{2\sigma_i^2}\right) \qquad (C21)$$

where σ_i^2 is again the total variance perpendicular to the relation and we have evaluated the integral in the rotated coordinates of the linear model, $\{x', y'\}$. Eq. C21 can be solved using the integral of the error function and substituting the relation $y' = \alpha'_{\mathrm{cut}} x' + \beta'_{\mathrm{cut}}$ where $\{\alpha'_{\mathrm{cut}}, \beta'_{\mathrm{cut}}\}$ describe the magnitude cut in the rotated coordinate system. Knowing $\theta_{\mathrm{cut}} = \arctan(\alpha_{\mathrm{cut}})$, it follows that

$$\alpha'_{\mathrm{cut}} = \tan(\theta_{\mathrm{cut}} - \theta) \qquad (C22)$$

$$\beta'_{\mathrm{cut}} = \beta_{\mathrm{cut}}[\cos\theta_{\mathrm{cut}} - \tan(\theta_{\mathrm{cut}} - \theta)\sin\theta_{\mathrm{cut}}] - \beta\cos\theta \quad (C23)$$

Thus Eq. C21 becomes

$$f_i = \left[\frac{x'}{2} + \left(\frac{\beta'_{\text{cut}}}{\alpha'_{\text{cut}}} + x' \right) \text{erf} \left(\frac{\alpha'_{\text{cut}} x' + \beta'_{\text{cut}}}{\sqrt{2}\sigma_i} \right) \right. \tag{C24}$$

$$\left. + \sqrt{\frac{2}{\pi}} \frac{\sigma_i}{b} \exp \left(-\frac{1}{2} \left(\frac{\alpha'_{\text{cut}} x' + \beta'_{\text{cut}}}{\sigma_i} \right)^2 \right) \right]_{x'_{\min}}^{x'_{\max}} \tag{C25}$$

Unlike Saglia et al. and La Barbera et al., we do *not* assign zero probability to objects with $m > m_{\text{cut}}$, but we scale p_i by the selection probability S_i. This accounts for the gradual nature of our magnitude cut.

For the Coma sample, there is no other obvious selection effect and S_i accurately describes the ratio of the spectroscopic sample to its parent distribution as a function of magnitude. However, the Abell 1689 data does suffer further selection effects which are not related to the magnitude cut above and should be corrected for. Firstly, only 60% of galaxies were selected per magnitude bin on average. Furthermore, we sample more than 60% of the most luminous galaxies due to low number statistics. Finally, we have the constraint that the data which enters the KR and FJR must have HST surface photometry, which further limits galaxies to be in the core of the cluster. Because of mass segregation, this biases the sample to more massive (luminous) galaxies. We calculate the ratio of the ideal sampling (given by S_i) to the actual sampling as a function of m which can be used as a weight w_i to correct for sampling effects, as in Saglia et al. (2001). Thus, accounting for the *cut* in magnitude with S_i and f_i, and additional selection effects as a function of magnitude with weights w_i, we can describe the frequency distribution of a single data point, given the model parameters to be

$$p'_{1,i} = \left[\frac{S_{1,i}}{f_{1,i}\sqrt{2\pi}\sigma_{1,i}} \exp \left(-\frac{\Delta_{1,i}^2}{2\sigma_{1,i}^2} \right) \right]^{w_i} \tag{C26}$$

The final likelihood for the model is thus

$$\mathcal{L}'_{\text{DLM}} = \sum_i p'_{1,i} + \sum_j p'_{2,j} \tag{C27}$$

where the two sums sum over the data of the two different populations.

Using the same MCMC set-up as before for this *double linear* model allows us to measure the *marginalised* offset between two scaling relations while fully accounting for magnitude cuts and selection effects.

C3   The Mixture Model

We can also describe a scaling relation using a double-Gaussian mixture model (Exercise 14 in Hogg et al.) in which we again have data $\{x_i, y_i\}$ with uncertainties $\{\sigma_{xi}, \sigma_{yi}\}$ that come *either* from a linear relation ($y = \alpha x + \beta$, model A, with *intrinsic* scatter σ_I) *or* another outlier distribution (model B with expectation value Y_b and intrinsic scatter σ_b) that overlaps that of the linear relation; thus bad data is modelled as coming from model B, whereas *good* data is modelled as coming from model A. The goal is to determine which data is good, and which bad. Say we have N data points and we don't know *a priori* which distribution(s) the data points are drawn from, but we assume it's either A or B. Model A is described by a normal distribution just

like the linear model (§C1),

$$p_{modelA} = \frac{1}{\sqrt{2\pi(\sigma_{\text{di}}^2 + \sigma_{\text{I}}^2)}} \exp \left[-\frac{\Delta_i^2}{2(\sigma_{\text{di}}^2 + \sigma_{\text{I}}^2)} \right] \tag{C28}$$

whereas model B is a simpler normal distribution

$$p_{\text{modelB}} = \frac{1}{\sqrt{2\pi(\sigma_{\text{di}}^2 + \sigma_b^2)}} \exp \left[-\frac{(y_i - Y_b)^2}{2(\sigma_{\text{di}}^2 + \sigma_b^2)} \right] \tag{C29}$$

Model B is described by just Y_b and σ_b, rather than any linear relation: it's just a scattering of points across all x, centred on Y_b.

We want to be able to reject data points when constructing the likelihood. Hogg et al. (2010) explain how this is achieved by a summation over a *mixture* of the linear distribution (model A) and the outlier distribution (model B)[10] such that the likelihood for the model is

$$\mathcal{L} = \prod_{i=1}^{N} [(1 - p_b).p_{\text{modelA}} + p_b.p_{\text{modelB}}] \tag{C30}$$

$$= \prod_{i=1}^{N} \frac{1 - p_b}{\sqrt{2\pi(\sigma_{\text{di}}^2 + \sigma_{\text{I}}^2)}} \exp \left(-\frac{\Delta_i^2}{2(\sigma_{\text{di}}^2 + \sigma_{\text{I}}^2)} \right)$$

$$+ \frac{p_b}{\sqrt{2\pi(\sigma_{di}^2 + \sigma_b^2)}} \exp \left(-\frac{(y_i - Y_b)^2}{2(\sigma_{di}^2 + \sigma_b^2)} \right)$$

where p_b is (a single parameter for) the probability of any given data point being bad. We again 'fit' the parameters $\theta, \beta', \sigma_I, p_b, Y_b, \sigma_b$, via MCMC sampling. The main advantage being a less subjective approach to removing outliers: we let the data and our knowledge of its uncertainty decide what to reject and what to keep. Again, the MCMC requires reasonably accurate initial guesses for the parameters to converge rapidly onto an acceptable result and such a guess can be provided by the 'maximum likelihood' estimates or by just being sensible.

---

[10] Recall that marginalisation is in essence a weighted sum over possible outcomes, where the weights are the respective probabilities

REFERENCES

Bañados E., Hung L.-W., De Propris R., West M. J., 2010, ApJ, 721, L14

Baade W., 1958, Ricerche Astronomiche, 5, 3

Barden M., Rix H.-W., Somerville R. S., Bell E. F., Häußler B., Peng C. Y., Borch A., Beckwith S. V. W., Caldwell J. A. R., Heymans C., Jahnke K., Jogee S., McIntosh D. H., Meisenheimer K., Sánchez S. F., Wisotzki L., Wolf C., 2005, ApJ, 635, 959

Barr J., Davies R., Jørgensen I., Bergmann M., Crampton D., 2005, AJ, 130, 445

Barr J., Jørgensen I., Chiboucas K., Davies R., Bergmann M., 2006, ApJ, 649, L1

Barrientos L. F., Schade D., Lopez-Cruz O., 1996, ApJ, 460, L89+

Bender R., Ziegler B., Bruzual G., 1996, ApJ, 463, L51

Bendinelli O., 1991, ApJ, 366, 599

Bendinelli O., Parmeggiani G., Zavatti F., 1982, Astrophysics & Space Sciences, 83, 239

Bernardi M., Sheth R. K., Annis J., Burles S., Eisenstein D. J., Finkbeiner D. P., Hogg D. W., Lupton R. H., et al. 2003, AJ, 125, 1866

Bertin E., Arnouts S., 1996, A&AS, 117, 393

Bessell M. S., 1990, PASP, 102, 1181

Bois M., Emsellem E., Bournaud F., Alatalo K., Blitz L., Bureau M., Cappellari M., Davies R. L., et al. 2011, MNRAS, 416, 1654

Bouwens R. J., Illingworth G. D., Blakeslee J. P., Broadhurst T. J., Franx M., 2004, ApJ, 611, L1

Bower R. G., Kodama T., Terlevich A., 1998, MNRAS, 299, 1193

Bower R. G., Lucey J. R., Ellis R. S., 1992, MNRAS, 254, 601

Broadhurst T., Takada M., Umetsu K., Kong X., Arimoto N., Chiba M., Futamase T., 2005, ApJ, 619, L143

Bruzual G., Charlot S., 2003, MNRAS, 344, 1000

Bruzual A. G., 1983, ApJ, 273, 105

Butcher H., Oemler Jr. A., 1984, ApJ, 285, 426

Butkevich A. G., Berdyugin A. V., Teerikorpi P., 2005, MNRAS, 362, 321

Cappellari M., 2002, MNRAS, 333, 400

Cappellari M., Bacon R., Bureau M., Damen M. C., Davies R. L., de Zeeuw P. T., Emsellem E., Falcón-Barroso J., Krajnović D., Kuntschner H., McDermid R. M., Peletier R. F., Sarzi M., van den Bosch R. C. E., van de Ven G., 2006, MNRAS, 366, 1126

Cappellari M., di Serego Alighieri S., Cimatti A., Daddi E., Renzini A., Kurk J. D., Cassata P., Dickinson M., Franceschini A., Mignoli M., Pozzetti L., Rodighiero G., Rosati P., Zamorani G., 2009, ApJ, 704, L34

Cappellari M., Emsellem E., 2004, PASP, 116, 138

Cardelli J. A., Clayton G. C., Mathis J. S., 1989, ApJ, 345, 245

Carretero C., Vazdekis A., Beckman J. E., 2007, MNRAS, 375, 1025

Cenarro A. J., Trujillo I., 2009, ApJ, 696, L43

Chiboucas K., Barr J., Flint K., Jørgensen I., Collobert M., Davies R., 2009, ApJS, 184, 271

Chung A., van Gorkom J. H., Kenney J. D. P., Crowl H., Vollmer B., 2009, AJ, 138, 1741

Ciotti L., 1991, A&A, 249, 99

Clemens M. S., Bressan A., Panuzzo P., Rampazzo R., Silva L., Buson L., Granato G. L., 2009, MNRAS, 392, 982

Cowie L. L., Songaila A., Hu E. M., Cohen J. G., 1996, AJ, 112, 839

de Vaucouleurs G., 1953, MNRAS, 113, 134

Djorgovski S., Davis M., 1987, ApJ, 313, 59

D'Onofrio M., Valentinuzzi T., Secco L., Caimmi R., Bindoni D., 2006, New Astronomy Reviews, 50, 447

Dressler A., Lynden-Bell D., Burstein D., Davies R. L., Faber S. M., Terlevich R., Wegner G., 1987, ApJ, 313, 42

Ebeling H., Voges W., Bohringer H., Edge A. C., Huchra J. P., Briel U. G., 1996, MNRAS, 281, 799

Ellis R. S., Smail I., Dressler A., Couch W. J., Oemler Jr. A., Butcher H., Sharples R. M., 1997, ApJ, 483, 582

Emsellem E., Cappellari M., Krajnović D., Alatalo K., Blitz L., Bois M., Bournaud F., Bureau M., et al. 2011, MNRAS, 414, 888

Emsellem E., Cappellari M., Krajnović D., van de Ven G., Bacon R., Bureau M., Davies R. L., de Zeeuw P. T., et al. 2007, MNRAS, 379, 401

Ettori S., De Grandi S., Molendi S., 2002, A&A, 391, 841

Faber S. M., Dressler A., Davies R. L., Burstein D., Lynden-Bell D., 1987, in S. M. Faber ed., Nearly Normal Galaxies. From the Planck Time to the Present Global scaling relations for elliptical galaxies and implications for formation. pp 175–183

Faber S. M., Jackson R. E., 1976, ApJ, 204, 668

Fakhouri O., Ma C.-P., Boylan-Kolchin M., 2010, MNRAS, 406, 2267

Fan L., Lapi A., De Zotti G., Danese L., 2008, ApJ, 689, L101

Ferguson H. C., Dickinson M., Giavalisco M., Kretchmer C., Ravindranath S., Idzi R., Taylor E., Conselice C. J., Fall S. M., Gardner J. P., Livio M., Madau P., Moustakas L. A., Papovich C. M., Somerville R. S., Spinrad H., Stern D., 2004, ApJ, 600, L107

Frei Z., Gunn J. E., 1994, AJ, 108, 1476

Fritz A., Jørgensen I., Schiavon R. P., Chiboucas K., 2009, Astronomische Nachrichten, 330, 931

Fritz A., Ziegler B. L., Bower R. G., Smail I., Davies R. L., 2005, MNRAS, 358, 233

Gavazzi R., Adami C., Durret F., Cuillandre J.-C., Ilbert O., Mazure A., Pelló R., Ulmer M. P., 2009, A&A, 498, L33

Gerhard O. E., 1993, MNRAS, 265, 213

Halkola A., Seitz S., Pannella M., 2006, MNRAS, 372, 1425

Hamabe M., Kormendy J., 1987, in P. T. de Zeeuw ed., Structure and Dynamics of Elliptical Galaxies Vol. 127 of IAU Symposium, Correlations Between R/1/4 - Law Parameters for Bulges and Elliptical Galaxies. pp 379–+

Hamilton D., 1985, ApJ, 297, 371

Han M., Mould J. R., 1992, ApJ, 396, 453

Harrison C. D., Colless M., Kuntschner H., Couch W. J., de Propris R., Pracy M. B., 2010, MNRAS, 409, 1455

Harrison C. D., Colless M., Kuntschner H., Couch W. J., de Propris R., Pracy M. B., 2011, MNRAS, 413, 1036

Hernquist L., Spergel D. N., Heyl J. S., 1993, ApJ, 416, 415

Hogg D. W., 1999, ArXiv Astrophysics e-prints

Hogg D. W., Baldry I. K., Blanton M. R., Eisenstein D. J., 2002, ArXiv Astrophysics e-prints

Hogg D. W., Bovy J., Lang D., 2010, ArXiv e-prints

Holden B. P., Blakeslee J. P., Postman M., Illingworth G. D., Demarco R., Franx M., Rosati P., Bouwens et al. 2005, ApJ, 626, 809

Holden B. P., van der Wel A., Franx M., Illingworth G. D., Blakeslee J. P., van Dokkum P., Ford H., Magee D., Postman M., Rix H.-W., Rosati P., 2005, ApJ, 620, L83

Holden B. P., van der Wel A., Kelson D. D., Franx M., Illingworth G. D., 2010, ApJ, 724, 714

Hook I. M., Jørgensen I., Allington-Smith J. R., Davies R. L., Metcalfe N., Murowinski R. G., Crampton D., 2004, PASP, 116, 425

Hopkins P. F., Bundy K., Croton D., Hernquist L., Keres D., Khochfar S., Stewart K., Wetzel A., Younger J. D., 2010, ApJ, 715, 202

Hopkins P. F., Bundy K., Hernquist L., Wuyts S., Cox T. J., 2010, MNRAS, 401, 1099

Hopkins P. F., Bundy K., Murray N., Quataert E., Lauer T. R., Ma C.-P., 2009, MNRAS, 398, 898

Hopkins P. F., Hernquist L., Cox T. J., Keres D., Wuyts S., 2009, ApJ, 691, 1424

Hopkins P. F., Lauer T. R., Cox T. J., Hernquist L., Kormendy J., 2009, ApJS, 181, 486

Jensen J. B., Tonry J. L., Luppino G. A., 1999, ApJ, 510, 71

Jørgensen I., 2009, PASA, 26, 17

Jørgensen I., Bergmann M., Davies R., Barr J., Takamiya M., Crampton D., 2005, AJ, 129, 1249

Jørgensen I., Chiboucas K., Flint K., Bergmann M., Barr J., Davies R., 2006, ApJ, 639, L9

Jørgensen I., Franx M., Hjorth J., van Dokkum P. G., 1999a, MNRAS, 308, 833

Jørgensen I., Franx M., Hjorth J., van Dokkum P. G., 1999b, MNRAS, 308, 833

Jørgensen I., Franx M., Kjaergaard P., 1992, A&AS, 95, 489

Jørgensen I., Franx M., Kjaergaard P., 1995a, MNRAS, 273, 1097

Jørgensen I., Franx M., Kjaergaard P., 1995b, MNRAS, 276, 1341

Jørgensen I., Franx M., Kjaergaard P., 1996, MNRAS, 280, 167

Kelson D. D., Illingworth G. D., van Dokkum P. G., Franx M., 2000, ApJ, 531, 184

Khochfar S., Emsellem E., Serra P., Bois M., Alatalo K., Bacon R., Blitz L., Bournaud F., et al. 2011, MNRAS,

417, 845

Khochfar S., Silk J., 2006, ApJ, 648, L21

Kodama T., Arimoto N., 1997, A&A, 320, 41

Komatsu E., Smith K. M., Dunkley J., Bennett C. L., Gold B., Hinshaw G., Jarosik N., Larson D., et al. 2011, ApJS, 192, 18

Kormendy J., 1977, ApJ, 218, 333

Krist J., Hook R., 1999, The Tiny Tim User's Guide.. STScI, 3700 San Martin Drive, Baltimore, MD 21218, USA., v6.3 edn

Kubo J. M., Stebbins A., Annis J., Dell'Antonio I. P., Lin H., Khiabanian H., Frieman J. A., 2007, ApJ, 671, 1466

La Barbera F., Busarello G., Merluzzi P., Massarotti M., Capaccioli M., 2003, ApJ, 595, 127

Landolt A. U., 1992, AJ, 104, 340

Landolt A. U., Uomoto A. K., 2007, AJ, 133, 768

Lemze D., Barkana R., Broadhurst T. J., Rephaeli Y., 2008, MNRAS, 386, 1092

Liu M. C., Graham J. R., 2001, ApJ, 557, L31

Lubin L. M., Sandage A., 2001, AJ, 122, 1084

Madau P., Ferguson H. C., Dickinson M. E., Giavalisco M., Steidel C. C., Fruchter A., 1996, MNRAS, 283, 1388

Madau P., Pozzetti L., Dickinson M., 1998, ApJ, 498, 106

Mahdavi A., Hoekstra H., Babul A., Henry J. P., 2008, MNRAS, 384, 1567

Maller A. H., Katz N., Kereš D., Davé R., Weinberg D. H., 2006, ApJ, 647, 763

Maraston C., 2005, MNRAS, 362, 799

Mason B. S., Myers S. T., 2000, ApJ, 540, 614

Maybhate A., et al. 2010, ACS Data Handbook. STScI, 3700 San Martin Drive, Baltimore, MD 21218, USA., v10.0 edn

McIntosh D. H., Bell E. F., Rix H.-W., Wolf C., Heymans C., Peng C. Y., Somerville R. S., Barden M., Beckwith S. V. W., Borch A., Caldwell J. A. R., Häußler B., Jahnke K., Jogee S., Meisenheimer K., Sánchez S. F., Wisotzki L., 2005, ApJ, 632, 191

Mehlert D., Thomas D., Saglia R. P., Bender R., Wegner G., 2003, A&A, 407, 423

Mei S., Holden B. P., Blakeslee J. P., Ford H. C., Franx M., Homeier N. L., Illingworth G. D., Jee M. J., Overzier R., Postman M., Rosati P., Van der Wel A., Bartlett J. G., 2009, ApJ, 690, 42

Méndez-Abreu J., Aguerri J. A. L., Corsini E. M., Simonneau E., 2008, A&A, 478, 353

Mieske S., Infante L., Benítez N., Coe D., Blakeslee J. P., Zekser K., Ford H. C., Broadhurst T. J., et al. 2004, AJ, 128, 1529

Mo H. J., Mao S., White S. D. M., 1998, MNRAS, 295, 319

Moffat A. F. J., 1969, A&A, 3, 455

Moran S. M., Ellis R. S., Treu T., Smail I., Dressler A., Coil A. L., Smith G. P., 2005, ApJ, 634, 977

Morandi A., Pedersen K., Limousin M., 2011, ApJ, 729, 37

Naab T., Johansson P. H., Ostriker J. P., 2009, ApJ, 699, L178

Naab T., Trujillo I., 2006, MNRAS, 369, 625

Oguri M., Takada M., Umetsu K., Broadhurst T., 2005, ApJ, 632, 841

Okabe N., Okura Y., Futamase T., 2010, ApJ, 713, 291

Pahre M. A., Djorgovski S. G., de Carvalho R. R., 1996, ApJ, 456, L79+

Patil A., Huard D., Fonnesbeck C. J., 2010, Journal of Sta-

tistical Software, 35, 1

Pavlovsky C., et al. 2004, ACS Instrument Handbook. STScI, 3700 San Martin Drive, Baltimore, MD 21218, USA., v5.0 edn

Peng E.-H., Andersson K., Bautz M. W., Garmire G. P., 2009, ApJ, 701, 1283

Price J., Phillipps S., Huxor A., Smith R. J., Lucey J. R., 2011, MNRAS, 411, 2558

Rakos K., Schombert J., Odell A., 2007, ApJ, 658, 929

Renzini A., Ciotti L., 1993, ApJ, 416, L49+

Riemer-Sørensen S., Paraficz D., Ferreira D. D. M., Pedersen K., Limousin M., Dahle H., 2009, ApJ, 693, 1570

Saglia R. P., Bertschinger E., Baggley G., Burstein D., Colless M., Davies R. L., McMahan Jr. R. K., Wegner G., 1993, MNRAS, 264, 961

Saglia R. P., Colless M., Burstein D., Davies R. L., McMahan R. K., Wegner G., 2001, MNRAS, 324, 389

Saglia R. P., Sánchez-Blázquez P., Bender R., Simard L., Desai V., Aragón-Salamanca A., Milvang-Jensen B., Halliday C., et al. 2010, A&A, 524, A6+

Sánchez-Blázquez P., Gorgas J., Cardiel N., González J. J., 2006, A&A, 457, 809

Sánchez-Blázquez P., Jablonka P., Noll S., Poggianti B. M., Moustakas J., Milvang-Jensen B., Halliday C., Aragón-Salamanca A., et al. 2009, A&A, 499, 47

Sandage A., 1972, ApJ, 176, 21

Santos Jr. J. F. C., Alloin D., Bica E., Bonatto C., 2001, VizieR Online Data Catalog, 3219, 0

Sarzi M., Falcón-Barroso J., Davies R. L., Bacon R., Bureau M., Cappellari M., de Zeeuw P. T., Emsellem E., Fathi K., Krajnović D., Kuntschner H., McDermid R. M., Peletier R. F., 2006, MNRAS, 366, 1151

Schade D., Barrientos L. F., Lopez-Cruz O., 1997, ApJ, 477, L17+

Schade D., Carlberg R. G., Yee H. K. C., Lopez-Cruz O., Ellingson E., 1996, ApJ, 464, L63+

Schlegel D. J., Finkbeiner D. P., Davis M., 1998, ApJ, 500, 525

Sérsic J. L., 1963, Boletin de la Asociacion Argentina de Astronomia La Plata Argentina, 6, 41

Sirianni M., Jee M. J., Benítez N., Blakeslee J. P., Martel A. R., Meurer G., Clampin M., De Marchi G., Ford H. C., Gilliland R., Hartig G. F., Illingworth G. D., Mack J., McCann W. J., 2005, PASP, 117, 1049

Smith J. A., Tucker D. L., Kent S., Richmond M. W., Fukugita M., Ichikawa T., Ichikawa S., Jorgensen A. M., et al. 2002, AJ, 123, 2121

Smith R. J., Lucey J. R., Hudson M. J., Allanson S. P., Bridges T. J., Hornschemeier A. E., Marzke R. O., Miller N. A., 2009, MNRAS, 392, 1265

Stanford S. A., Eisenhardt P. R., Dickinson M., 1998, ApJ, 492, 461

Stanford S. A., Eisenhardt P. R. M., Dickinson M., 1995, ApJ, 450, 512

Stott J. P., Collins C. A., Burke C., Hamilton-Morris V., Smith G. P., 2011, MNRAS, 414, 445

Struble M. F., Rood H. J., 1999, ApJS, 125, 35

Teerikorpi P., 1997, ARA&A, 35, 101

Terlevich A. I., Caldwell N., Bower R. G., 2001, MNRAS, 326, 1547

Terlevich A. I., Kuntschner H., Bower R. G., Caldwell N., Sharples R. M., 1999, MNRAS, 310, 445

Thomas D., Maraston C., Bender R., Mendes de Oliveira C., 2005, ApJ, 621, 673

Thomsen B., Baum W. A., Hammergren M., Worthey G., 1997, ApJ, 483, L37+

Tinsley B. M., Gunn J. E., 1976, ApJ, 203, 52

Tolman R. C., 1930, Proceedings of the National Academy of Science, 16, 511

Trager S. C., Faber S. M., Dressler A., 2008, MNRAS, 386, 715

Treu T., Stiavelli M., Bertin G., Casertano S., Møller P., 2001, MNRAS, 326, 237

Trujillo I., Aguerri J. A. L., Cepa J., Gutiérrez C. M., 2001a, MNRAS, 321, 269

Trujillo I., Aguerri J. A. L., Cepa J., Gutiérrez C. M., 2001b, MNRAS, 328, 977

Trujillo I., Conselice C. J., Bundy K., Cooper M. C., Eisenhardt P., Ellis R. S., 2007, MNRAS, 382, 109

Valdes F., Gupta R., Rose J. A., Singh H. P., Bell D. J., 2004, ApJS, 152, 251

van der Marel R. P., Franx M., 1993, ApJ, 407, 525

van der Marel R. P., van Dokkum P. G., 2007, ApJ, 668, 756

van der Wel A., Franx M., van Dokkum P. G., Huang J., Rix H.-W., Illingworth G. D., 2006, ApJ, 636, L21

van der Wel A., Franx M., van Dokkum P. G., Rix H.-W., Illingworth G. D., Rosati P., 2005, ApJ, 631, 145

van der Wel A., Holden B. P., Zirm A. W., Franx M., Rettura A., Illingworth G. D., Ford H. C., 2008, ApJ, 688, 48

van Dokkum P. G., Ellis R. S., 2003, ApJ, 592, L53

van Dokkum P. G., Franx M., 1996a, MNRAS, 281, 985

van Dokkum P. G., Franx M., 1996b, MNRAS, 281, 985

van Dokkum P. G., Franx M., Kelson D. D., Illingworth G. D., 1998, ApJ, 504, L17+

van Dokkum P. G., Franx M., Kelson D. D., Illingworth G. D., 2001, ApJ, 553, L39

van Dokkum P. G., Kriek M., Franx M., 2009, Nature, 460, 717

van Dokkum P. G., van der Marel R. P., 2007, ApJ, 655, 30

Wegner G., Colless M., Baggley G., Davies R. L., Bertschinger E., Burstein D., McMahan Jr. R. K., Saglia R. P., 1996, ApJS, 106, 1

Willick J. A., 1994, ApJS, 92, 1

Worthey G., 1994, ApJS, 95, 107

Ziegler B. L., Bower R. G., Smail I., Davies R. L., Lee D., 2001, MNRAS, 325, 1571

Ziegler B. L., Saglia R. P., Bender R., Belloni P., Greggio L., Seitz S., 1999, A&A, 346, 13

Ziegler B. L., Thomas D., Böhm A., Bender R., Fritz A., Maraston C., 2005, A&A, 433, 519